They admitted principally within 14 days of symptom onset. Cerebral infarction was diagnosed by clinical course, neurological examinations, and CT or MRI. TIA was diagnosed based on the Classification of Cerebrovascular Diseases III from the National Institute of Neurological Disorders and Stroke (13). Clinical indication for TEE was made mainly for the detection of embolic sources by an independent attending physician. Two-dimensional and RT 3D-TEE were performed to assess any embolic sources such as intracardiac thrombus, right-to-left shunt, and complicated atherosclerotic changes of the aortic arch. Patients with an evident embolic source such as chronic AF, significant valvular heart disease, a prosthetic heart valve or mitral valve repair, or those with technically inadequate echocardiographic studies were excluded. Informed consent for RT 3D-TEE was obtained from all patients. The following information was obtained from the medical records of each patient: age, sex, vascular risk factors (systemic hypertension, dyslipidemia, diabetes mellitus, and cigarette smoking), extracranial and intracranial large artery atherosclerosis defined as greater than 50% stenosis or occlusion, previous stroke, congestive heart failure, and the left atrial diameter (LAD) measured by transthoracic echocardiography. According to the Oxfordshire Community Stroke Project (OCSP) criteria, patients were classified from their clinical symptoms by two experienced neurologists into four categories, as having total anterior circulation stroke, partial anterior circulation stroke, posterior circulation stroke, or lacunar stroke. The neurologists were blinded to the neuroimaging and vascular imaging results.

The presence of PAF was defined as a history of PAF diagnosed previously or newly diagnosed by continuous ECG monitoring for at least several days after admission or 24-hour Holter ECG monitoring during hospitalization. Patients were allocated to a group with PAF (PAF group) or a group without PAF (non-PAF group). The diagnosis of PAF was based on a history of PAF or recurrent episodes of AF lasting for more than 30 s documented by continuous ECG monitoring or 24-hour Holter ECG monitoring. This study is a retrospective analysis of our prospective stroke registry and was approved by the institutional review committee at the National Cerebral and Cardiovascular Center.

Two- and three-dimensional transesophageal echocardiography

RT 3D-TEE was performed using a commercially available iE 33 Ultrasound machine and fully sampled X7-2t TEE transducer (Philips Medical Systems, Andover, MA, USA). Routine 2D TEE and RT 3D-TEE examinations were performed using the same transducer.

LAA flow velocity was measured by pulsed-wave Doppler echocardiographic interrogation at the orifice of the LAA. The presence of a patent foramen ovale based on the detection using saline contrast technique and atherosclerotic changes of the aorta were assessed with 2D TEE. Atherosclerotic changes of the aorta were defined as ≥4 mm thick, or with mobile components of plaques of the aorta.The scan volume was the wide-angled acquisition mode that included the LAA and surrounding structures acquired at the maximal frame rate. This 3D Full volume mode had high time resolution and provided ECG-gated acquisition of a large 3D volume created from subvolumes stitched together and synchronized to a single cardiac cycle. To avoid stitch artifacts, special care was taken to stabilize the probe during data acquisition. The acquisition was repeated whenever obvious artifacts were found. Images were reviewed online to ensure adequate 3D visualization of the LAA.

Three-dimensional data analysis

Images were digitally stored for subsequent offline analysis using QLAB 7·0 software (Philips Medical Systems). LAA volumes are measured using the multiplanar reconstruction mode of the General Imaging 3D Quantification plug-in to visualize LAA in the three different dimensions. Offline 3D analysis was performed by personnel who were blinded to the clinical information. The image was rotated in order to provide a long-axis view of the LAA (Fig. 1a) and to allow simultaneous visualization of the LAA orifice in the short-axis view (Fig. 1b). The LAA orifice was determined by two lines: one was drawn between the vestibule of the mitral valve annulus near the left coronary artery and the lateral ledge of the left superior pulmonary vein, and the other was drawn between a point near the aortic valve annulus and the left superior pulmonary vein limbus (11,14,15). Using the Stacked Contours mode in the software, a line was drawn from the LAA orifice to the apex, and then 15 short-axis multiplanar slices of the LAA from the orifice to the apex were automatically generated. By manual tracing the LAA contour in each slice (Fig. 1c), a virtual 3D image was automatically created from the stacking of multiple slices, and the volume of the LAA was calculated (Fig. 1d).

LAA end-diastolic volume was measured just before the *P* wave in the ECG and the end-systolic volume was measured at the QRS

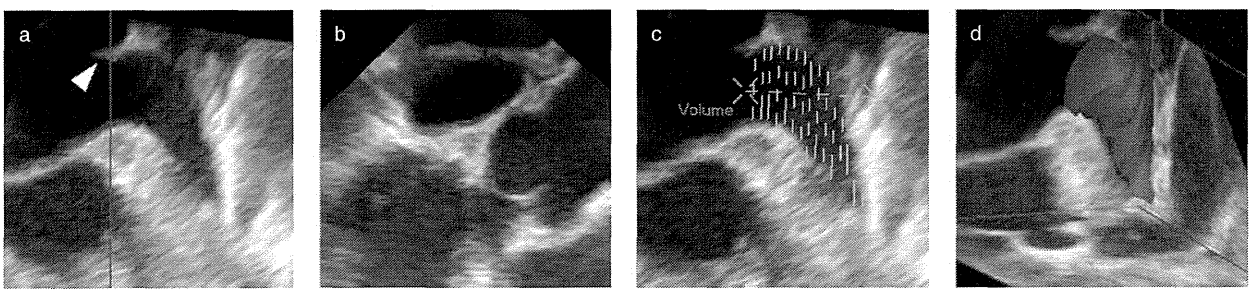

Fig. 1 Offline measurement of the left atrial appendage (LAA). (a) LAA long-axis view at the level of the mitral valve annulus, and lateral ridge of the left superior pulmonary vein (white arrowhead). (b) LAA orifice in the short-axis view. (c) The long-axis view of the LAA that results from the stacking of multiple short-axis segments. (d) By manually tracing the endocardial border of the individual short-axis segments, a virtual three-dimensional image of the LAA is obtained that can be used to calculate the LAA volume.

© 2014 The Authors.
International Journal of Stroke © 2014 World Stroke Organization

complex (5). Volumetric data were corrected by area of the body surface based on the Du Bois formula (end-diastolic volume index, end-systolic volume index). LAA-EF was calculated using the following equation: LAA-EF = [(end-diastolic volume – end-systolic volume) * 100]/end-diastolic volume (%).

Statistical analysis

Statistical analysis was performed using JMP 8·0 statistical software (SAS Institute Inc, Cary, NC, USA). Continuous data are expressed as mean ± standard deviation. Categorical data are presented as absolute numbers (percentages). Differences in continuous variables between two groups were assessed using a Student's *t*-test or Mann–Whitney *U*-test, as appropriate. Differences in categorical variables between two groups were assessed using a chi-square test or Fisher's exact test, as appropriate. Observer variability was assessed by the coefficient of variation, and the concordance correlation coefficient for TEE-derived measurements repeating the analysis at least one-month later by the same observer who performed the first analysis and by a second independent blinded observer. Correlations between two variables were evaluated by linear regression analysis. To evaluate the ability of LAA flow velocity, end-diastolic volume index, end-systolic volume index, and LAA-EF to predict PAF, receiver operating characteristic (ROC) curves were constructed. The c-statistic (area under the ROC curve) was used as a scalar measure to assess the performance of each parameter. The c-statistics for different parameters were compared by a nonparametric method (16). To determine whether each TEE parameter was associated with PAF, multivariate logistic regression analysis was performed. The multivariate logistic regression model was adjusted for, age, sex, and variables with a probability value <0·1 in univariate analysis to assess the independent impact of each cutoffs of TEE parameter on PAF. Probability values <0·05 were considered significant.

Results

Between July 2010 and November 2012, a total of 150 patients were referred for RT 3D-TEE. Four patients were excluded because we were unable to insert a probe in two patients, and it was difficult to view the LAA in the other two patients. The remaining 146 patients underwent RT 3D-TEE without complications. Among them, 102 patients (73 men, mean age 72·2 ± 10·7 years) were in NSR at the time of TEE and were included in this study. The other 44 patients including 43 with chronic AF and 1 with a prosthetic mitral valve and AF at the TEE examination were excluded. Twenty-three patients were allocated to the PAF group, and 79 to the non-PAF group. The baseline characteristics of each group are listed in Table 1. Diabetes mellitus was less frequent in patients with than without PAF (4% vs. 25%, $P = 0·038$). OCSP categories were not different in the groups.

The intraobserver and interobserver correlation coefficients for LAA volume measurement were 0·900 and 0·861, respectively; and the interclass correlation coefficients were 0·891 and 0·847, respectively. The imaging characteristics derived from echocardiography are shown in Table 2. Patients with PAF tended to have larger LAD (39·3 ± 5·9 mm vs. 36·3 ± 7·7 mm, $P = 0·086$), lower LAA flow velocity (46·1 ± 27·3 cm/s vs. 66·3 ± 24·2 cm/s, $P < 0·001$), larger end-diastolic volume index (4·78 ± 3·00 ml/m^2 vs. 3·14 ± 2·04 ml/m^2, $P = 0·003$) and end-systolic volume index (3·10 ± 2·47 ml/m^2 vs. 1·39 ± 1·56 ml/m^2, $P < 0·001$), and lower LAA-EF (37·3 ± 19·1% vs. 57·1 ± 17·5%, $P < 0·001$) than those without PAF.

The correlations between each TEE parameter are shown in Fig 2. The end-diastolic volume index was strongly correlated with the end-systolic volume index, and was moderately correlated with the LAA flow velocity and LAA-EF.

ROC curve analysis showed that the optimal cutoff value of the LAA flow velocity to predict PAF was 39·0 cm/s, with a c-statistic

Table 1 Baseline clinical characteristics

Characteristics	Total (n = 102)	PAF (n = 23)	non-PAF (n = 79)	P value
Sex, men, n (%)	73 (72)	15 (65)	58 (73)	0·443
Age (years)	72·2 ± 10·7	73·7 ± 9·0	71·8 ± 11·2	0·654
Body surface area (m^2)	1·59 ± 0·17	1·59 ± 0·21	1·59 ± 0·16	0·935
Hypertension, n (%)	72 (71)	14 (61)	58 (73)	0·245
Diabetes mellitus, n (%)	21 (21)	1 (4)	20 (25)	0·038
Dyslipidemia, n (%)	58 (57)	12 (52)	46 (58)	0·606
Smoking, n (%)	20 (20)	3 (13)	17 (22)	0·368
Congestive heart failure, n (%)	6 (6)	1 (4)	5 (6)	0·772
Previous stoke, n (%)	26 (25)	2 (9)	24 (30)	0·054
Extracranial large artery atherosclerosis, n (%)	13 (13)	2 (9)	11 (14)	0·727
Intracranial large artery atherosclerosis, n (%)	29 (28)	8 (35)	21 (27)	0·443
Clinical subtypes				
Total anterior circulation stroke, n (%)	10 (10)	1 (4)	9 (11)	0·232
Partial anterior circulation stroke, n (%)	26 (25)	10 (43)	16 (20)	
Posterior circulation stroke, n (%)	27 (26)	5 (22)	22 (28)	
Lacunar stroke, n (%)	38 (37)	7 (30)	31 (39)	
Unclassified, n (%)	1 (1)	0 (0)	1 (1)	

Continuous values are reported as the mean ± SD. PAF, paroxysmal atrial fibrillation.

© 2014 The Authors.
International Journal of Stroke © 2014 World Stroke Organization

Table 2 Echocardiographic parameters

Characteristics	Total ($n = 102$)	PAF ($n = 23$)	non-PAF ($n = 79$)	P value
Left atrial diameter (mm)	37·0 ± 7·5	39·3 ± 5·9	36·3 ± 7·7	0·086
*Patent foramen ovale, n (%)	36 (41)	3 (23)	33 (44)	0·225
Atherosclerotic changes at the aorta, n (%)	37 (36)	6 (26)	31 (39)	0·327
LAA flow velocity (cm/s)	61·8 ± 26·1	46·1 ± 27·3	66·3 ± 24·2	<0·001
End diastolic volume (ml)	5·52 ± 3·68	7·98 ± 5·16	4·90 ± 2·93	0·006
End-diastolic volume index (ml/m²)	3·51 ± 2·38	4·78 ± 3·00	3·14 ± 2·04	0·003
End-systolic volume (ml)	2·78 ± 2·98	5·00 ± 4·14	2·13 ± 2·18	<0·001
End-systolic volume index (ml/m²)	1·78 ± 1·93	3·10 ± 2·47	1·39 ± 1·56	<0·001
LAA-EF (%)	52·6 ± 19·6	37·3 ± 19·1	57·1 ± 17·5	<0·001

*Data on patent foramen ovale was available in 13 patients of the PAF group and 75 of the non-PAF group.
Continuous values are reported as the mean ± SD. PAF, paroxysmal atrial fibrillation; LAA, left atrial appendage; EF, ejection fraction.

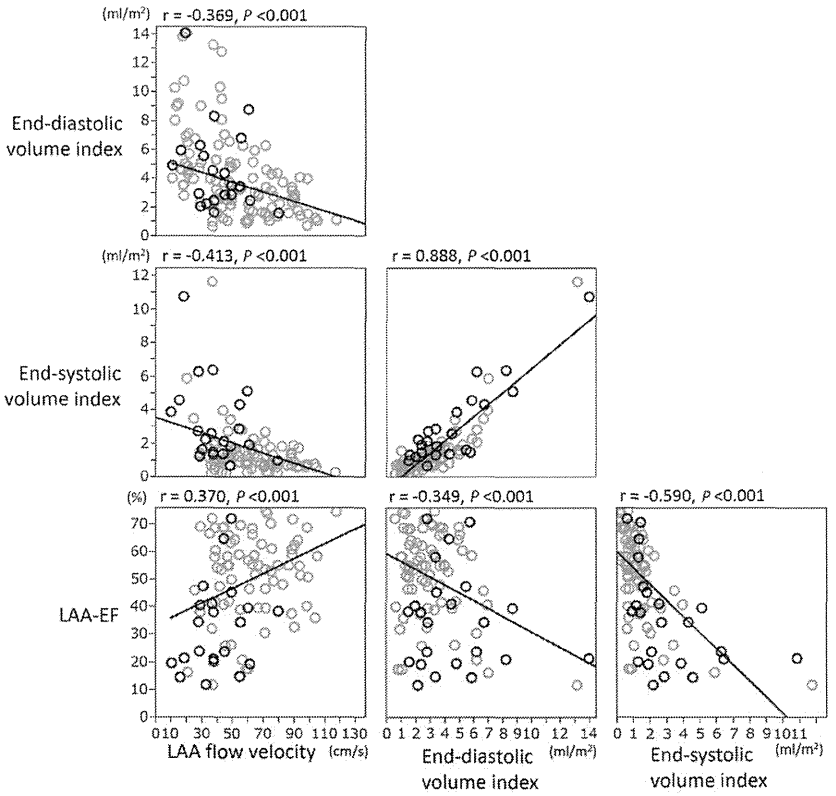

Fig. 2 Relations between transesophageal echocardiographic parameters. Regression lines among all subjects are shown. Black open circles = patients with paroxysmal atrial fibrillation (AF); Gray open circles = patients without AF.

of 0·762. The cutoff values of the end-diastolic volume index and the end-systolic volume index were 4·52 ml/m² and 1·26 ml/m², with c-statistics of 0·694 and 0·806, respectively. The cutoff of LAA-EF was 47·9%, with a c-statistic of 0·774 (Table 3, Fig. 3). There was a significant difference in the c-statistics among the four TEE-derived parameters ($P = 0·007$), and the end-systolic volume index was superior to the end-diastolic volume index for predicting PAF ($P = 0·007$).

In multivariate analysis, the LAA flow velocity ≤39·0 cm/s (odds ratio 12·91, 95% CI 3·70–53·90), the end-diastolic volume index ≥4·52 ml/m² (odds ratio 4·03, 95% CI 1·36–12·44), the end-systolic volume index ≥1·26 ml/m² (odds ratio 13·37, 95% CI 3·40–89·75), and LAA-EF ≤47·9% (odds ratio 10·02, 95% CI 3·33–35·34) were independently associated with PAF after adjusting for age, sex, and a history of diabetes mellitus, and previous stroke (Table 4).

Discussion

In this study, we determined the association between LAA volumetric parameters assessed by RT 3D-TEE and PAF in patients with acute cerebral infarction or TIA. This is the first report to show the association between LAA volumetric parameters and the presence of PAF in patients with acute stroke, although some 2D

© 2014 The Authors.
International Journal of Stroke © 2014 World Stroke Organization

Table 3 Receiver-operating-characteristic curve analysis of 3D-TEE parameters for predicting PAF

Variable	c-Statistic (95% CI)	Optimal cutoff	Sensitivity	Specificity	PPV	NPV
LAA flow velocity (cm/s)	0·762 (0·622–0·862)	≤39·0	54·6	89·7	60·0	87·5
End-diastolic volume index (ml/m²)	0·694 (0·565–0·798)	≥4·52	47·8	82·3	44·0	84·4
End-systolic volume index (ml/m²)	0·806 (0·696–0·883)	≥1·26	91·3	60·3	40·4	96·0
LAA-EF (%)	0·774 (0·635–0·871)	≤47·9	78·3	74·7	47·3	92·2

3D-TEE, three dimensional transesophageal echocardiography; CI, confidence interval; EF, ejection fraction; LAA, left atrial appendage; NPV, negative predictive value; PAF, paroxysmal atrial fibrillation; PPV, positive predictive value.

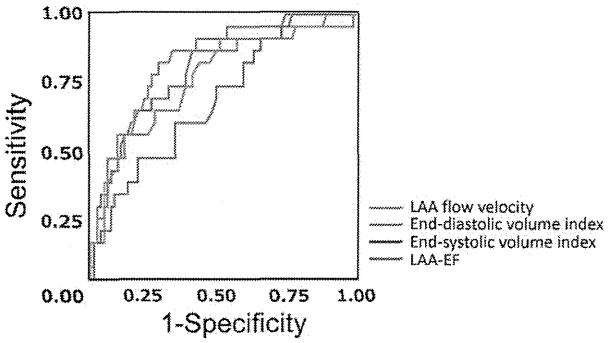

Fig. 3 Receiver operating characteristic curves comparing transesophageal echocardiographic parameters for the prediction of paroxysmal atrial fibrillation. Curves are shown for the left atrial appendage (LAA) flow velocity, end-diastolic volume index, end-systolic volume index, and LAA ejection fraction (EF).

Table 4 Multivariate logistic regression analysis of 3D-TEE parameters for predicting PAF

Variable	Odds ratio (95% CI)	*P* value
LAA flow velocity ≤39·0 cm/s	12·91 (3·70–53·90)	<0·001
End-diastolic volume index ≥4·52 ml/m²	4·03 (1·36–12·44)	0·010
End-systolic volume index ≥1·26 ml/m²	13·37 (3·40–89·75)	<0·001
LAA-EF ≤47·9%	10·02 (3·33–35·34)	<0·001

The regression model was adjusted for age, sex, diabetes mellitus, and previous stroke. 3D-TEE, three-dimensional transesophageal echocardiography; CI, confidence interval; EF, ejection fraction; LAA, left atrial appendage; PAF, paroxysmal atrial fibrillation.

parameters on LAA are known predictors for PAF. The first major finding was that LAA volumetric parameters as well as low LAA flow velocity were independently associated with the presence of PAF. The second finding was that not only a large LAA volume but also reduced EF was significantly associated with PAF. Third, the LAA end-systolic volume seems to be superior to the end-diastolic volume for detecting PAF in acute stroke patients. Finally, the intraobserver and interobserver variabilities for LAA volume assessment were excellent.

A large LAA volume, low EF and low flow velocity were independently associated with the presence of PAF in patients with acute cerebral infarction or TIA in the present study. Taguchi *et al.* (8) reported a significant difference in the LAA flow velocity between acute stroke patients with and without PAF (34·7 ± 9·3 cm/s vs. 64·0 ± 12·1 cm/s). In 2D- and 3D-TEE in patients without stroke, a large 2D LAA area (5) and large 3D LAA volume (11) were found to be significantly association with the presence of AF. Nucifora *et al.* (17) reported a progressive increase in LAA orifice size on RT 3D-TEE with an increasing frequency of AF in patients that were candidates for LAA closure endotherapy. Recently, Shimizu *et al.* (18) reported the correlation between LAA-EF derived from 2D-TEE area measurement and PAF in acute stroke patients. In their report, LAA-EF could predict PAF more accurate than the LAA flow velocity. There are several reports regarding LAA volumetric comparison between patients with AF and those with NSR in the absence of stroke (11,19). Chen *et al.* (12) reported lower LAA-EF in 62 patients with AF (24 ± 14%) than that in 34 with NSR (38 ± 17%, $P < 0·01$). Their LAA-EF value in patients with NSR was relatively low compared with ours (57·1 ± 17·5%). This difference is most likely due to the time resolution of 3D image acquisition. Compared with the 3D Zoom mode, the 3D Full volume mode provides higher time resolution and allows more accurate measurements of the end-diastolic and end-systolic volumes, and LAA-EF based on the ECG.

After spontaneous conversion of AF, diminishment of LAA function was reported as LAA 'stunning' (20). The persistence of AF produces changes in atrial function and structure, electrical remodeling, structural remodeling and contractile remodeling as there is reduced contraction and dilatation of the left atrium (21). The end-systolic volume appeared to be most sensitive parameter to detect contractile remodeling, since it reflects systolic dysfunction of a dilated LAA in patients with PAF, even if they return to NSR. Although LAA-EF and the LAA flow velocity are widely used to evaluate contractile function, they might not be appropriate for detecting volume enlargement of LAA. In contrast, the end-diastolic volume directly reflects volume enlargement, but is not useful to evaluate contraction of LAA. The end-systolic volume appears to indicate both volume enlargement and reduced contraction of LAA. However, a direct comparison of these parameters in multivariate analysis is difficult because of the strong correlations.

Our method is feasible for the measurement of LAA volume because of low interobserver and intraobserver variability. In order to analyze LAA volumes precisely based on the ECG, we investigated only patients with NSR at the time of TEE. We used the 3D Full volume mode, and this mode can be used only in patients with a regular cardiac rhythm. This mode provides 3D images with adequate width and depth and has high time resolution. On the other hand, the 3D Zoom mode is commonly used

© 2014 The Authors.
International Journal of Stroke © 2014 World Stroke Organization

for patients in AF. The time resolution of the routine 3D Zoom mode is reduced by increasing the area of interest. Because ECG gating is not applicable with the 3D Zoom mode, ECG-based analysis with reduced time resolution may be unreliable. LAA flow velocity can be measured easily by 2D-TEE; however, LAA flow velocity was reported to vary about 1·5 times from the measurement site of the LAA orifice or apex (22). In contrast, our LAA volumetric evaluation with high time resolution seems to be consistent and reproducible. Classification of LAA morphology may also enable us to assess the risk of ischemic stroke, but it is still controversial (23,24).

This study had several limitations and our results could not be readily compared with previous reports. First, there was a risk of statistical error because of the small number of patients. Second, this study was not performed for all the consecutive stroke patients, because TEE is an invasive procedure and is not well-tolerated in patients with a poor general condition. Therefore there may be a selection bias. Third, continuous ECG monitoring and 24-hour Holter ECG monitoring during hospitalization might have failed to detect PAF. This leaves the possibility that PAF may be present in some of patients in the non-PAF group. Longer ECG monitoring, such as 7-day Holter ECG monitoring and outpatient telemetry monitoring (25,26), might have improved PAF detection and that may enable for further assessment of the correlations between TEE parameters and duration or frequency of PAF. Fourth, echocardiographic parameters in patients with PAF would not be different from those without PAF if we underwent TEE without recent PAF-attack because of the lack of a recovery effect from LAA stunning. A large prospective cohort study is needed to confirm the association between the LAA volumetric parameters and PAF in patients with acute cerebral infarction or TIA.

Conclusions

LAA function appeared to be impaired in patients with PAF, even though RT 3D-TEE was performed during NSR. Three-dimensional analysis of the LAA is a promising method for detecting PAF in patients with acute cerebral infarction or TIA.

Acknowledgement

The authors thank Dr Yoshifumi Wakata, Medical Information Center, Kyushu University Hospital, for advice on the statistical analyses.

References

1 Wolf PA, Abbott RD, Kannel WB. Atrial fibrillation as an independent risk factor for stroke: the Framingham Study. *Stroke* 1991; **22:**983–8.
2 Roy D, Marchand E, Gagné P, Chabot M, Cartier R. Usefulness of anticoagulant therapy in the prevention of embolic complications of atrial fibrillation. *Am Heart J* 1986; **112:**1039–43.
3 Stahrenberg R, Edelmann F, Haase B *et al.* Transthoracic echocardiography to rule out paroxysmal atrial fibrillation as a cause of stroke or transient ischemic attack. *Stroke* 2011; **42:**3643–5.
4 Okada Y, Shibazaki K, Kimura K, Iguchi Y, Miki T. Brain natriuretic peptide as a predictor of delayed atrial fibrillation after ischaemic stroke and transient ischaemic attack. *Eur J Neurol* 2010; **17:**326–31.
5 Pollick C, Taylor D. Assessment of left atrial appendage function by transesophageal echocardiography. Implications for the development of thrombus. *Circulation* 1991; **84:**223–31.
6 García-Fernández MA, Torrecilla EG, San Román D *et al.* Left atrial appendage Doppler flow patterns: implications on thrombus formation. *Am Heart J* 1992; **124:**955–61.
7 Pozzoli M, Febo O, Torbicki A *et al.* Left atrial appendage dysfunction: a cause of thrombosis? Evidence by transesophageal echocardiography-Doppler studies. *J Am Soc Echocardiogr* 1991; **4:**435–41.
8 Taguchi Y, Takashima S, Hirai T *et al.* Significant impairment of left atrial function in patients with cardioembolic stroke caused by paroxysmal atrial fibrillation. *Intern Med* 2010; **49:**1727–32.
9 Shah SJ, Bardo DM, Sugeng L *et al.* Real-time three-dimensional transesophageal echocardiography of the left atrial appendage: initial experience in the clinical setting. *J Am Soc Echocardiogr* 2008; **21:**1362–8.
10 Kumar V, Nanda NC. Is it time to move on from two-dimensional transesophageal to three-dimensional transthoracic echocardiography for assessment of left atrial appendage? Review of existing literature. *Echocardiography* 2012; **29:**112–6.
11 Nakajima H, Seo Y, Ishizu T *et al.* Analysis of the left atrial appendage by three-dimensional transesophageal echocardiography. *Am J Cardiol* 2010; **106:**885–92.
12 Chen OD, Wu WC, Jiang Y, Xiao MH, Wang H. Assessment of the morphology and mechanical function of the left atrial appendage by real-time three-dimensional transesophageal echocardiography. *Chin Med J* 2012; **125:**3416–20.
13 Special report from the National Institute of Neurological Disorders and Stroke. Classification of cerebrovascular diseases III. *Stroke* 1990; **21:**637–76.
14 Budge LP, Shaffer KM, Moorman JR, Lake DE, Ferguson JD, Mangrum JM. Analysis of in vivo left atrial appendage morphology in patients with atrial fibrillation: a direct comparison of transesophageal echocardiography, planar cardiac CT, and segmented three-dimensional cardiac CT. *J Interv Card Electrophysiol* 2008; **23:**87–93.
15 Cabrera JA, Ho SY, Climent V, Sánchez-Quintana D. The architecture of the left lateral atrial wall: a particular anatomic region with implications for ablation of atrial fibrillation. *Eur Heart J* 2008; **29:**356–62.
16 DeLong ER, DeLong DM, Clarke-Pearson DL. Comparing the areas under two or more correlated receiver operating characteristic curves: a nonparametric approach. *Biometrics* 1988; **44:**837–45.
17 Nucifora G, Faletra FF, Regoli F *et al.* Evaluation of the left atrial appendage with real-time 3-dimensional transesophageal echocardiography: implications for catheter-based left atrial appendage closure. *Circ Cardiovasc Imaging* 2011; **4:**514–23.
18 Shimizu T, Takada T, Shimode A *et al.* Association between paroxysmal atrial fibrillation and the left atrial appendage ejection fraction during sinus rhythm in the acute stage of stroke: a transesophageal echocardiographic study. *J Stroke Cerebrovasc Dis* 2013; **22:**1370–6.
19 Valocik G, Kamp O, Mihciokur M *et al.* Assessment of the left atrial appendage mechanical function by three-dimensional echocardiography. *Eur J Echocardiogr* 2002; **3:**207–13.
20 Grimm RA, Leung DY, Black IW, Stewart WJ, Thomas JD, Klein AL. Left atrial appendage 'stunning' after spontaneous conversion of atrial fibrillation demonstrated by transesophageal Doppler echocardiography. *Am Heart J* 1995; **130:**174–6.
21 Allessie M, Ausma J, Schotten U. Electrical, contractile and structural remodeling during atrial fibrillation. *Cardiovasc Res* 2002; **54:**230–46.
22 Goldberg YH, Gordon SC, Spevack DM, Gordon GM. Disparities in emptying velocity within the left atrial appendage. *Eur J Echocardiogr* 2010; **11:**290–5.
23 Di Biase L, Santangeli P, Anselmino M *et al.* Does the left atrial appendage morphology correlate with the risk of stroke in patients with atrial fibrillation? Results from a multicenter study. *J Am Coll Cardiol* 2012; **60:**531–8.

© 2014 The Authors.
International Journal of Stroke © 2014 World Stroke Organization

24 Ren JF, Callans DJ, Marchlinski FE. Letter. What is the natural relationship between left atrial appendage morphology and history of stroke? *J Am Coll Cardiol* 2013; **61**:689–90.
25 Stahrenberg R, Weber-Krüger M, Seegers J *et al.* Enhanced detection of paroxysmal atrial fibrillation by early and prolonged continuous Holter monitoring in patients with cerebral ischemia presenting in sinus rhythm. *Stroke* 2010; **41**:2884–8.
26 Kamel H, Navi BB, Elijovich L *et al.* Pilot randomized trial of outpatient cardiac monitoring after cryptogenic stroke. *Stroke* 2013; **44**:528–30.

© 2014 The Authors.
International Journal of Stroke © 2014 World Stroke Organization

◆原　著◆　　脳卒中36: 260–265, 2014

リアルタイム3次元経食道心臓超音波検査を用いた急性期虚血性脳血管障害における左心耳の3次元評価

田中　弘二[1)]　古賀　政利[2)]　大山　賢[1)]　徳永　敬介[1)]
佐藤　和明[1)]　鈴木理恵子[1)]　峰松　一夫[1)]　豊田　一則[1)]

要旨：【目的】急性期脳梗塞，一過性脳虚血発作における左心耳の3次元評価項目と心房細動(AF)の関連を明らかにする．【方法】リアルタイム3次元経食道心臓超音波検査を行った127例(年齢74±11歳，男性88例)を持続性AF 33例，発作性AF 22例，AFなし72例の3群に分け検討した．【結果】持続性AF，発作性AF，AFなし各群で入口部面積(5.73±1.95 cm^2，4.45±2.42 cm^2，3.23±1.47 cm^2，$p<0.001$)，深さ(3.42±0.71 cm，2.95±0.89 cm，2.61±0.70 cm，$p<0.001$)，体積(11.37±6.33 cm^3，7.59±5.03 cm^3，4.90±2.92 cm^3，$p<0.001$)いずれも有意差を認めた．多変量解析でも入口部面積，体積はAFと有意に関連していた．【結論】急性期虚血性脳血管障害で左心耳の拡大は持続性ないし発作性AFの存在と関連していた．

Key words: real-time three-dimensional transesophageal echocardiography, left atrial appendage, ischemic stroke, atrial fibrillation

はじめに

経食道心臓超音波検査(transesophageal echocardiography; TEE)は脳血管障害における塞栓源の検索に有用である[1)]．心房細動(atrial fibrillation; AF)によって左心耳(left atrial appendage; LAA)内に形成される心腔内血栓は心原性脳塞栓症の主要な原因であり，TEEでは通常体表からの超音波検査では評価が困難とされるLAAの詳細な観察が可能である[2)]．

AFでは電気的(electrical)リモデリング，構造的(structural)リモデリングに加え，左心房およびLAAの拡張，収縮力低下などの機械的(contractile)リモデリングによって，LAAの機能低下が生じる[3)]．以前より2次元(two-dimensional; 2D) TEEにおいて，LAAの長軸断面積がAF症例で有意に大きいことが報告されている[4)]．しかしLAAは解剖学的に複雑な構造をしている場合があり，2D断面のみの観察ではしばしば正確な評価が困難である[5)]．近年，リアルタイム3次元(real-time three-dimensional; RT 3D) TEEによってLAAの3次元的な形態評価が可能となり，さらに検査時に3Dデータセットを記録することでオフラインでの任意の断面，角度での観察や体積の測定が可能となっている[6,7)]．

虚血性脳血管障害の急性期にAFを発見することは適切な二次予防の観点から重要である．今回，我々は左心耳の3D評価項目とAFとの関連を明らかにするため，急性期脳梗塞もしくは一過性脳虚血発作(transient ischemic attack; TIA)の症例を対象にRT 3D-TEEを用いてLAAの3D評価を行い，AFとの関連を調べた．

方　法

1. 対象

2010年7月から2012年11月までに国立循環器病研究センター脳血管内科に入院し，同意が得られRT 3D-TEEを施行した発症14日以内の急性期脳梗塞，TIAの連続例を対象に後方視的に調査した．脳梗塞の診断は臨床症状と診察所見，頭部CTないしMRI画像所見をもとに診断し，TIAはNational Institute of Neurological Disorders and Strokeの分類第III版に基づいて診断した[8)]．RT 3D-TEEは通常の2D-TEEと同様に心腔内血栓，卵円孔開存を介した右左短絡，弁膜症や弁に付着する異常構造物，大動脈の複合粥腫病変など脳梗塞の原因となりうる塞栓源の検索を目的に行った．

臨床情報は診療録を参照し，年齢，性別，血管危険因子(高血圧，脂質異常症，糖尿病，現在の喫煙)ならびにAF，今回のイベント前の脳梗塞の既往，うっ血性心不全の有無，入院時より直近の血清脳性ナトリウム利尿ペプチド(brain natriuretic peptide; BNP)値(正常値≤17 pg/ml)を調べた．また身長，体重から体表面積をDu Boisの式を用いて計算した．

本研究では，各症例をAFの頻度に応じて以下の3群に分

[1)]国立循環器病研究センター脳血管内科
[2)]同　脳卒中集中治療科
(2013年11月14日受付，2013年12月18日受理)

Presented by Medical*Online

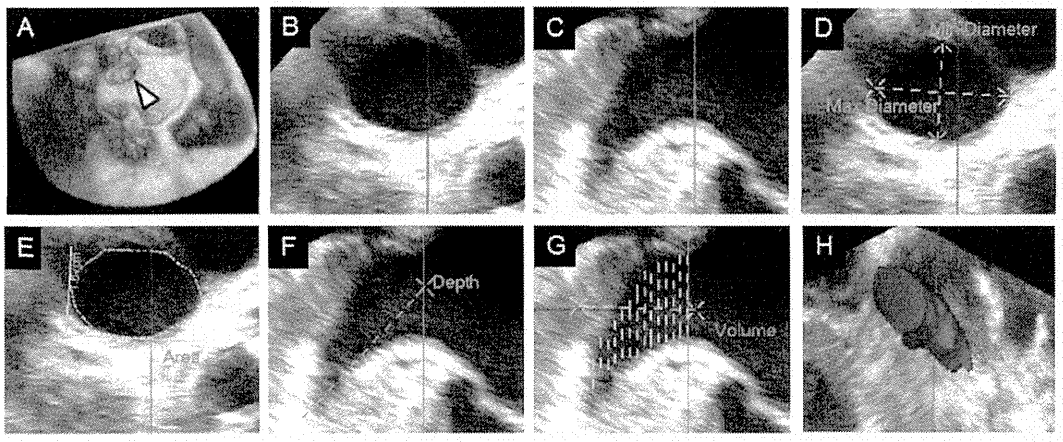

Fig. 1　オフラインでの左心耳(LAA)の計測
(A)LAA(矢頭)の3次元画像での正面像．(B)LAA短軸断面．(C)LAA長軸断面．(D)LAA入口部の長径，短径．(E)入口部面積．(F)LAAの深さ．(G)入口部から先端までを15の短軸断面に分けたLAA長軸像．(H)手動トレースした各短軸断面をもとに構築されたLAAの3次元形状モデル．

類した．1．入院時より心電図上AFを認め，持続性のもの(chronic AF; C-AF群)．2．発作性AFの既往ないし入院中に心電図上30秒以上持続する発作性AFを認めた群(paroxysmal AF; P-AF群)，3．AFの既往がなく入院経過中にもAFを認めなかった群(non-AF群)．これら3群間で，臨床的特徴やRT 3D-TEEによるLAA所見を比較した．本研究は当院の倫理委員会の承認を得て行った．

2．評価方法

検査にはiE 33超音波診断装置とX7-2t TEEトランスジューサ(Philips Medical Systems, Andover, MA, USA)を用いた．RT-3D TEEによる評価は通常の2D-TEEの手技に連続して行った．LAA血流速度はLAAの入口部でパルスドプラ法を用いて測定した．LAAの3Dデータセットの記録には3D zoom modeを用いた(Fig. 1A)．なおデータ取得時にはLAAを含むできるだけ小さい関心領域を設定するようにした．

画像の解析はQLAB 7.0(Philips Medical Systems)を用いて行った．LAAの評価は記録時に洞調律の症例では心電図上のP波の直前，AFの症例ではLAAが最大となる時相で測定した．まずGeneral Imaging 3D Quantificationプラグインを用いて複数断面表示を行い，LAAの長軸ならびに短軸断面(Fig. 1B，C)を表示し，LAAの入口部を決定した．LAAの入口部はそれぞれ左上肺静脈開口部のlateral ridgeと大動脈弁輪，僧帽弁輪を結ぶ直線を基準に決定し[9-11]，短軸断面においてLAA入口部の長径，短径を計測し(Fig. 1D)，長径/短径比を求めた．さらにフリーハンドツールを用いて入口部面積を測定した(Fig. 1E)．次に長軸断面においてLAA入口部からLAA先端部までの距離をLAAの深さとして測定した(Fig. 1F)．体積の測定はStacked Contours modeを用いて，LAAの入口部から先端部までを入口部と並行する15の短軸断面に分け(Fig. 1G)，それぞれの短軸断面におけるLAA内腔を手動でトレースし，体積を自動計算した(Fig. 1H)．バイアスを避けるため画像解析は臨床情報を参照せずに行った．また，無作為に選択した10例において複数検者でLAAの体積を測定し，級内相関係数を算出した．

統計処理にはJMP 9.0(SAS Institute Inc, Cary, NC, USA)を用いた．名義変数の比較ではχ^2検定を用いた．連続変数は3群間で一元配置分散分析を用い，解析結果が統計学的有意であった場合にはpost hoc検定としてTukeyのhonestly significant difference法を用いて検討した．またLAAの入口部面積，体積と以下の項目[性別，年齢，体表面積，高血圧，糖尿病，脂質異常症，現在の喫煙，AF(C-AF，P-AF，non-AF各群に分類)，脳梗塞の既往，うっ血性心不全]の関連を評価するために単回帰分析，重回帰分析を用いた．なお，重回帰分析には性別，年齢と単回帰分析でp値<0.05の項目を共変数として使用した．測定値は例数(%)または平均値±標準偏差で示し，p値<0.05を統計学的有意とした．

結　果

全体で146例に対してRT 3D-TEEを施行し，そのうち発症2週間以内に入院した脳梗塞，TIAは135例であった．検査時に3D zoom modeによるLAAのデータセット取得が不十分であった8例を除外し，最終的に127例(年齢73.5±10.8歳，男性88人)を対象とした．このうち，33例がC-AF群，22例がP-AF群，72例がnon-AF群に分類された．本研究の対象において認められたAFは全例，非弁膜症性AFであり，P-AF群は検査時には全例が洞調律であった．

各群の背景因子をTable 1に示す．3群間で年齢(p=0.041)，うっ血性心不全の有無(p=0.006)，血清BNP値(p=0.006)に有意差を認め，C-AF群は高齢で，うっ血性心不全を有する頻度が高く，血清BNPが高い傾向がみられた．次にTable 2にLAAの各評価項目を示す．LAAの体積における級内相関係数は0.829であった．3群間の比較ではLAA

Presented by Medical*Online

Table 1　患者背景

項目	全体(n=127)	C-AF群(n=33)	P-AF群(n=22)	non-AF群(n=72)	p値
性別，男性，n(%)	88(69.2)	22(66.7)	14(63.6)	52(72.2)	0.695
年齢(歳，平均±SD)	73.5±10.8	77.4±8.7	73.4±9.1	71.7±11.7	0.041
体表面積(m^2，平均±SD)	1.59±0.17	1.58±0.15	1.59±0.21	1.59±0.17	0.971
高血圧，n(%)	88(69.2)	24(72.7)	13(59.1)	51(70.8)	0.525
糖尿病，n(%)	28(22.1)	9(27.3)	1(4.6)	18(25.0)	0.090
脂質異常症，n(%)	65(51.2)	15(45.5)	11(50.0)	39(54.2)	0.704
現在の喫煙，n(%)	21(16.5)	3(9.1)	2(9.1)	16(22.2)	0.143
脳梗塞の既往，n(%)	29(22.9)	7(21.2)	1(4.6)	21(29.2)	0.533
うっ血性心不全，n(%)	15(11.9)	9(27.3)	1(4.6)	5(6.9)	0.006
血清 BNP*(pg/ml，平均±SD)	164.1±279.5	287.4±235.7	175.7±141.1	100.5±312.8	0.006

SD; standard deviation, BNP; brain natriuretic peptide
*データの得られなかったnon-AF群の4例を除外して計算した．

Table 2　LAA評価項目

項目	全体(n=127)	C-AF群(n=33)	P-AF群(n=22)	non-AF群(n=72)	p値
LAA血流速度(cm/s，平均±SD)	51.8±27.4	27.7±16.5	46.1±28.0	64.7±22.9	<0.001
入口部長径(cm，平均±SD)	2.74±0.60	3.08±0.56	2.94±0.71	2.58±0.47	<0.001
入口部短径(cm，平均±SD)	1.91±0.54	2.26±0.47	2.09±0.51	1.69±0.47	<0.001
長径/短径比(平均±SD)	1.48±0.26	1.37±0.13	1.43±0.27	1.54±0.29	0.008
入口部面積(cm^2，平均±SD)	4.08±2.07	5.73±1.95	4.45±2.42	3.23±1.47	<0.001
深さ(cm，平均±SD)	2.88±0.81	3.42±0.71	2.95±0.89	2.61±0.70	<0.001
体積(cm^3，平均±SD)	7.05±5.18	11.37±6.33	7.59±5.03	4.90±2.92	<0.001

LAA; left atrial appendage, SD; standard deviation

血流速度(27.7±16.5 cm/s，46.1±28.0 cm/s，64.7±22.9 cm/s，p<0.001)，長径(3.08±0.56 cm，2.94±0.71 cm，2.58±0.47 cm，p<0.001)，短径(2.26±0.47 cm，2.09±0.51 cm，1.69±0.47 cm，p<0.001)，長径/短径比(1.37±0.13，1.43±0.27，1.54±0.29，p=0.008)，入口部面積(5.73±1.95 cm^2，4.45±2.42 cm^2，3.23±1.47 cm^2，p<0.001)，深さ(3.42±0.71 cm，2.95±0.89 cm，2.61±0.70 cm，p<0.001)，体積(11.37±6.33 cm^3，7.59±5.03 cm^3，4.90±2.92 cm^3，p<0.001)のいずれにおいても有意差を認めた．さらにpost hock検定で各項目を比較すると，入口部長径ならびに短径はC-AF群とnon-AF群，P-AF群とnon-AF群の間で有意差があり(Fig. 2A，B)，長径/短径比と深さはC-AF群とnon-AF群の間で有意差があり(Fig. 2C，E)，入口部面積および体積はすべての群間で有意差を認めた(Fig. 2D，F)．

LAAの入口部面積，体積との関連を調べた単回帰分析，重回帰分析の結果をTable 3に示す．単回帰分析ではLAAの入口部面積とは年齢，AF，うっ血性心不全の有無で，LAAの体積とはAF，うっ血性心不全の有無の間で関連がみられた．重回帰分析を行った結果，LAAの入口部面積では年齢とAF，うっ血性心不全の有無の間で有意な関連がみられ，体積ではAFのみ独立して関連がみられた(p<0.001)．

考　察

2D-TEEでLAAを後方視的に評価する場合，従来は検査中に記録された2D画像を解析するしかなかったが，その画像がLAAの最もよく見える2D画像(best 2D view)であるかどうかの保証はなかった．また検査時にLAA入口部や長軸断面のbest 2D viewを検証しながら順番に記録していくことは検査時間の延長につながり現実的ではない．それに対して，RT 3D-TEEは検査時に記録したデータセットを読み込むことでいつでもbest 2D viewの画像も含め表示，解析することが可能である．

RT 3D-TEEで記録したデータセットによるLAAの3D画像は，造影CTの再構成画像とよく相関し[6]，LAAの体積はAF症例で有意に大きいことが報告されている[11-13]．しかし，虚血性脳血管障害の症例を対象とした検討はこれまで行われていない．Nuciforaら[13]は，AFが発作性，持続性，治療抵抗性となるにしたがってLAAの長径，短径，深さ，入口部面積が大きくなり，長径/短径比が小さくなることを報告したが，AFのない症例と発作性AF症例の間では有意差がなかった．それに対し本検討では長径，短径，入口部面積および体積でnon-AF群とP-AF群の間でも有意差を認め

Presented by Medical*Online

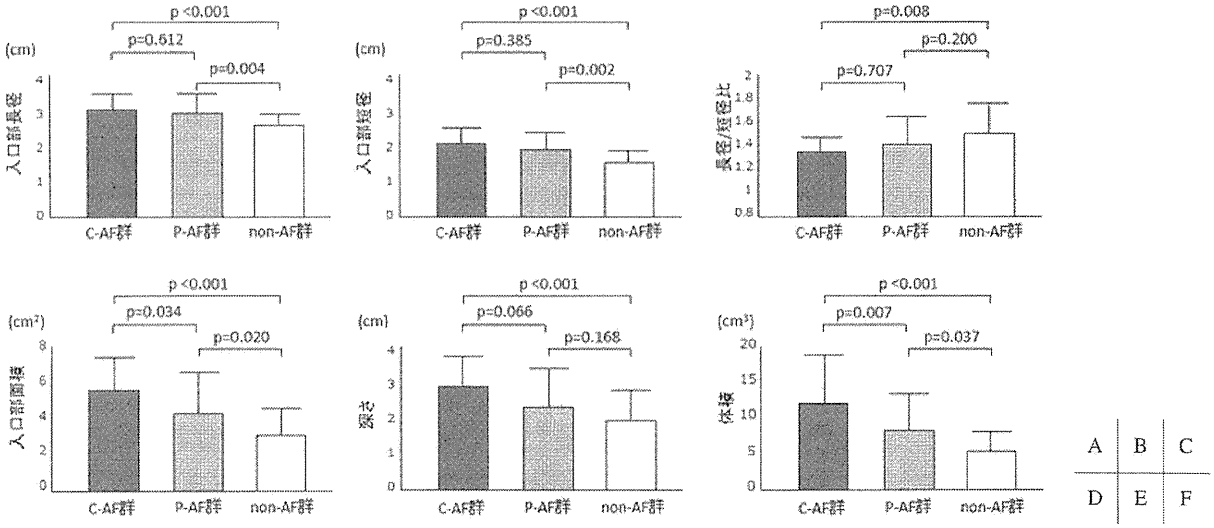

Fig. 2　C-AF群，P-AF群，non-AF群における左心耳(LAA)の入口部長径(A)，短径(B)，長径/短径比(C)，入口部面積(D)，深さ(E)，体積(F)の比較

Table 3　単回帰分析ならびに重回帰分析

	入口部面積				体積			
	単回帰分析		重回帰分析		単回帰分析		重回帰分析	
項目	β	p値	β	p値	β	p値	β	p値
性別*	0.064	0.486	−0.0055	0.944	0.076	0.398	0.033	0.675
年齢(歳)	0.26	0.004	0.17	0.033	0.15	0.085	0.041	0.603
体表面積(m^2)	−0.12	0.206			−0.035	0.698		
AF†		<0.001		<0.001		<0.001		<0.001
発作性AF	0.29		0.22		0.31		0.20	
持続性AF	0.58		0.44		0.58		0.50	
高血圧*	0.020	0.826			−0.061	0.492		
糖尿病*	−0.060	0.513			0.0020	0.982		
脂質異常症*	0.028	0.760			−0.014	0.878		
現在の喫煙*	0.026	0.776			0.016	0.860		
脳梗塞の既往*	−0.038	0.678			−0.056	0.531		
うっ血性心不全*	0.26	0.004	0.17	0.035	0.25	0.005	0.12	0.124
			調整済み R^2	0.29			調整済み R^2	0.27

AF; atrial fibrillation
*性別は男性=0，女性=1，他の変数は，なし=0，あり=1とした．
†単回帰分析，重回帰分析ともAFなしをコントロールとした．

た．その理由として，AF症例においてLAAの入口部面積や体積の拡大が虚血性脳血管障害の発症と関連することが報告されており[14,15]，本研究は虚血性脳血管障害の症例を対象にしていることから，本研究における発作性AF症例が特にLAAの拡大した集団であった可能性，また発症の前後でAFとなっていたために急性期には洞調律復帰後もAFによる電気的，機械的リモデリングの影響が残存する，いわゆるLAAのスタンニングの状態が持続していた可能性が考えられる[16,17]．さらに本研究でも長径/短径比がC-AF群で低く，LAAの入口部が円形に近いことが示されたが，僧房弁閉鎖不全による容量負荷で左心房の長径/短径比や縦径×2/(前後径+左右径)比が低下して1に近づくとの報告[18,19]，拡張型心筋症において左心室の縦径/横径比が低下して1に近づくとの報告があり[20]，LAA入口部の長径/短径比の低下もLAAの収縮力低下や容量負荷に起因していると予想される．本研究結果から，将来的にRT-3D TEEを用いたLAAの

Presented by Medical*Online

3D評価によって，洞調律の急性期虚血性脳血管障害における発作性AFの存在を予測することが可能となるかもしれない．

本研究ではC-AF群とP-AF群の間でもLAAの体積，入口部面積に有意差を認めた．AFは発作性であっても持続性であっても脳梗塞発症のリスクは同等と報告されており[21]，LAAの拡大のみが血栓形成に直接関与するわけではなく，LAA血流速度[4,22,23]，LAAの形状[24,25]，などの複合的な要因が関与していると推察される．これらの項目やLAAの3D評価項目とLAA内血栓との関連，さらにBNP[26]などのバイオマーカーとの関連については今後検討が必要である．また近年議論されているLAAの形状の分類とAFに伴う脳梗塞発症頻度の関連はCT，MRIを利用したものであるが，今後RT 3D-TEEでも同様の解析が進むことが期待される．

今回解析に用いた3D zoom modeは心電図同期の必要なく画面上の任意の3D領域のデータセット取得が可能であるが，関心領域を広げるにつれて時間分解能が低下してしまう．一方，もう一つの取得方法である3D full volume modeは心電図に同期して広範囲の3Dデータをサブボリュームに分けて数拍かけて記録する手法で，広い関心領域で高い時間分解能を保持することができる．しかしデータ記録中の不整脈や呼吸，体動などによってアーティファクトが生じるため，洞調律の症例にしか用いることができず，データ取得時には適宜息止めを行い，適当な3Dデータセットが記録できているかどうかを確認する必要がある．現在，我々は洞調律の症例を対象とした3D full volume modeで取得した3Dデータの解析を行っている．

本研究における limitation として，まずTEEは侵襲的な検査であり，急性期脳梗塞，TIAの連続例に行うことは難しく，当院における急性期脳血管障害例へのTEEの適応は塞栓源検索やLAA内血栓の確認を目的としており，すでに心原性以外の原因が明らかな場合には積極的な適応としておらず，また全身状態の悪い症例には施行しにくいため，検査時点で選択バイアスが生じている可能性がある．次に，今回解析の対象とした3D zoom modeは時間分解能が低いために，LAAが最大となる時相を確実に捉えることができていない可能性がある．さらに，今回P-AF群は全例検査時に洞調律であったが，解析時には心電図を参照することから，検査時に洞調律であった症例とAFであった症例の間で情報バイアスが生じている可能性がある．

RT 3D-TEEによるLAAの3D評価において，急性期虚血性脳血管障害ではAFの存在がLAAの体積，入口部面積の拡大や，LAA入口部の長径/短径比の低下と関連することが示唆された．

本論文に関連しては，開示すべきCOI状態にある企業，組織，団体はいずれも存在しない．

謝　辞

本研究は独立行政法人日本学術振興会の科学研究費助成事業の助成(24591084)を受けて行った．

参考文献

1) Kapral MK, Silver FL: Preventive health care, 1999 update: 2. Echocardiography for the detection of a cardiac source of embolus in patients with stroke. Canadian Task Force on Preventive Health Care. CMAJ 161: 989–996, 1999
2) Seward JB, Khandheria BK, Oh JK, et al: Transesophageal echocardiography: technique, anatomic correlations, implementation, and clinical applications. Mayo Clin Proc 63: 649–680, 1988
3) Allessie M, Ausma J, Schotten U: Electrical, contractile and structural remodeling during atrial fibrillation. Cardiovasc Res 54: 230–246, 2002
4) Pollick C, Taylor D: Assessment of left atrial appendage function by transesophageal echocardiography. Implications for the development of thrombus. Circulation 84: 223–231, 1991
5) Veinot JP, Harrity PJ, Gentile F, et al: Anatomy of the normal left atrial appendage: a quantitative study of age-related changes in 500 autopsy hearts: implications for echocardiographic examination. Circulation 96: 3112–3115, 1997
6) Shah SJ, Bardo DM, Sugeng L, et al: Real-time three-dimensional transesophageal echocardiography of the left atrial appendage: initial experience in the clinical setting. J Am Soc Echocardiogr 21: 1362–1368, 2008
7) Lang RM, Mor-Avi V, Sugeng L, et al: Three-dimensional echocardiography: the benefits of the additional dimension. J Am Coll Cardiol 48: 2053–2069, 2006
8) Special report from the National Institute of Neurological Disorders and Stroke. Classification of cerebrovascular diseases III. Stroke 21: 637–676, 1990
9) Budge LP, Shaffer KM, Moorman JR, et al: Analysis of in vivo left atrial appendage morphology in patients with atrial fibrillation: a direct comparison of transesophageal echocardiography, planar cardiac CT, and segmented three-dimensional cardiac CT. J Interv Card Electrophysiol 23: 87–93, 2008
10) Cabrera JA, Ho SY, Climent V, et al: The architecture of the left lateral atrial wall: a particular anatomic region with implications for ablation of atrial fibrillation. Eur Heart J 29: 356–362, 2008
11) Nakajima H, Seo Y, Ishizu T, et al: Analysis of the left atrial appendage by three-dimensional transesophageal echocardiography. Am J Cardiol 106: 885–892, 2010
12) Chen OD, Wu WC, Jiang Y, et al: Assessment of the morphology and mechanical function of the left atrial appendage by real-time three-dimensional transesophageal echocardiography. Chin Med J 125: 3416–3420, 2012
13) Nucifora G, Faletra FF, Regoli F, et al: Evaluation of the left atrial appendage with real-time 3-dimensional transesophageal echocardiography: implications for catheter-based left atrial appendage closure. Circ Cardiovasc Imaging 4: 514–523, 2011
14) Beinart R, Heist EK, Newell JB, et al: Left atrial appendage dimensions predict the risk of stroke/TIA in patients with atrial fibrillation. J Cardiovasc Electrophysiol 22: 10–15, 2011
15) Burrell LD, Horne BD, Anderson JL, et al: Usefulness of left atrial appendage volume as a predictor of embolic stroke in patients with atrial fibrillation. Am J Cardiol 112: 1148–1152,

Presented by Medical*Online

2013
16) Fatkin D, Kuchar DL, Thorburn CW, et al: Transesophageal echocardiography before and during direct current cardioversion of atrial fibrillation: evidence for "atrial stunning" as a mechanism of thromboembolic complications. J Am Coll Cardiol 23: 307–316, 1994
17) Grimm RA, Leung DY, Black IW, et al: Left atrial appendage "stunning" after spontaneous conversion of atrial fibrillation demonstrated by transesophageal Doppler echocardiography. Am Heart J 130: 174–176, 1995
18) Maiello M, Sharma RK, Matteo CM, et al: Differential left atrial remodeling in LV diastolic dysfunction and mitral regurgitation. Echocardiography 26: 772–778, 2009
19) Yi JE, Chung WB, Cho JS, et al: Left atrial eccentricity in chronic mitral regurgitation: relation to left atrial function. Eur Heart J Cardiovasc Imaging 14: 110–117, 2013
20) Harjai KJ, Edupuganti R, Nunez E, et al: Does left ventricular shape influence clinical outcome in heart failure? Clin Cardiol 23: 813–819, 2000
21) Roy D, Marchand E, Gagné P, et al: Usefulness of anticoagulant therapy in the prevention of embolic complications of atrial fibrillation. Am Heart J 112: 1039–1043, 1986
22) Pozzoli M, Febo O, Torbicki A, et al: Left atrial appendage dysfunction: a cause of thrombosis? Evidence by transesophageal echocardiography-Doppler studies. J Am Soc Echocardiogr 4: 435–441, 1991
23) García-Fernández MA, Torrecilla EG, San Román D, et al: Left atrial appendage Doppler flow patterns: implications on thrombus formation. Am Heart J 124: 955–961, 1992
24) Di Biase L, Santangeli P, Anselmino M, et al: Does the left atrial appendage morphology correlate with the risk of stroke in patients with atrial fibrillation? Results from a multicenter study. J Am Coll Cardiol 60: 531–538, 2012
25) Kimura T, Takatsuki S, Inagawa K, et al: Anatomical characteristics of the left atrial appendage in cardiogenic stroke with low CHADS2 scores. Heart Rhythm 10: 921–925, 2013
26) Shimizu H, Murakami Y, Inoue S, et al: High plasma brain natriuretic polypeptide level as a marker of risk for thromboembolism in patients with nonvalvular atrial fibrillation. Stroke 33: 1005–1010, 2002

Abstract

Evaluation of the left atrial appendage by real-time three-dimensional transesophageal echocardiography for acute stroke patients

Koji Tanaka, M.D.,[1] Masatoshi Koga, M.D.,[2] Satoshi Ohyama, M.D.,[1] Keisuke Tokunaga, M.D.,[1] Kazuaki Sato, M.D.,[1] Rieko Suzuki, M.D.,[1] Kazuo Minematsu, M.D.,[1] and Kazunori Toyoda, M.D.[1]

[1]Department of Cerebrovascular Medicine, National Cerebral and Cardiovascular Center
[2]Department of Stroke Care Unit, National Cerebral and Cardiovascular Center

Background and Purpose: Atrial fibrillation (AF) causes remodeling of the left atrium and the left atrial appendage (LAA) that can lead to cardioembolic stroke. We investigated the association between the LAA parameters, measured using real-time three-dimensional transesophageal echocardiography (RT 3D-TEE), and the presence of AF in patients with acute ischemic stroke.

Methods: We performed RT 3D-TEE for patients with acute cerebral infarction or transient ischemic attack, measuring LAA orifice area, depth, and volume offline. Patients were classified as having chronic AF (C-AF group) or paroxysmal AF (P-AF group) or not having AF (non-AF group).

Results: Of 127 patients (mean age 74±11 years, 88 men), 33 were assigned to the C-AF group, 22 to the P-AF group, and 72 to the non-AF group. LAA orifice area (5.73±1.95 cm^2, 4.45±2.42 cm^2, and 3.23±1.47 cm^2, respectively; $p<0.001$), eccentricity index (1.54±0.29, 1.43±0.27, and 1.37±0.13, respectively; $p=0.008$), depth (3.42±0.71 cm, 2.95±0.89 cm, and 2.61±0.70 cm, respectively; $p<0.001$), and volume (11.37±6.33 cm^3, 7.59±5.03 cm^3, and 4.90±2.92 cm^3, respectively; $p<0.001$) were significantly different between groups. Post-hoc analysis revealed that only LAA orifice area and volume were useful in discriminating the three groups and that both were largest in C-AF group and smallest in non-AF group. After adjustment for sex, age, and congestive heart failure, LAA orifice area and volume were independently associated with the presence of AF.

Conclusion: Paroxysmal and chronic AF may contribute to the enlargement of both LAA orifice area and volume in patients with acute ischemic stroke.

Key words: real-time three-dimensional transesophageal echocardiography, left atrial appendage, ischemic stroke, atrial fibrillation

(Jpn J Stroke 36: 260–265, 2014)

Presented by Medical*Online

Ultrasonics 59 (2015) 94–101

Contents lists available at ScienceDirect

Ultrasonics

journal homepage: www.elsevier.com/locate/ultras

Substantial fluctuation of acoustic intensity transmittance through a bone-phantom plate and its equalization by modulation of ultrasound frequency

Osamu Saito [a], Zuojun Wang [a], Hidetaka Mitsumura [b], Takeki Ogawa [c], Yasuyuki Iguchi [b], Masayuki Yokoyama [a,*]

[a] Division of Medical Engineering, Research Center for Medical Sciences, The Jikei University School of Medicine, 3-25-8, Nishi-shinbashi, Minato-ku, Tokyo 105-8461, Japan
[b] Department of Neurology, The Jikei University School of Medicine, 3-25-8, Nishi-shinbashi, Minato-ku, Tokyo 105-8461, Japan
[c] Department of Emergency Medicine, The Jikei University School of Medicine, 3-25-8, Nishi-shinbashi, Minato-ku, Tokyo 105-8461, Japan

ARTICLE INFO

Article history:
Received 11 October 2014
Received in revised form 20 December 2014
Accepted 28 January 2015
Available online 7 February 2015

Keywords:
Acute ischemic stroke
Modulation
Sonothrombolysis
Thrombolysis
Transcranial transmittance

ABSTRACT

For safe and efficient sonothrombolysis therapies, accurate estimation of ultrasound transmittance through the human skull is essential. The present study clarifies uncertainty surrounding this transmittance and experimentally verifies the equalization of transmittance through the modulation of ultrasound frequency. By changing three factors (ultrasound frequency, the thickness of a bone-phantom plate, and the distance between a transducer and a bone-phantom plate), we measured the intensity of ultrasound passing through the plate. Two activating methods, sinusoidal waves at 500 kHz and modulated waves, were compared. When we changed (1) the distance between a transducer and a bone-phantom plate and (2) the thickness of the bone-phantom plate, ultrasound transmittance through the plates substantially fluctuated. The substantial fluctuation in transmittance was observed also for a cut piece of human temporal skull bone. This fluctuation significantly declined for the modulated wave. In conclusion, modulation of ultrasound frequency can equalize the transmittance with an approximately 30–65% fluctuation drop and an approximately 40% fluctuation drop for a bone-phantom plate and for a cut piece of skull bone, respectively. By using modulated waves, we can develop safer and more effective sonothrombolysis therapies.

© 2015 Elsevier B.V. All rights reserved.

1. Introduction

Advancements in therapies for acute ischemic strokes are critical in present-day medicine. Among the available therapies, administration of a recombinant tissue plasminogen activator (rt-PA) is the first choice, and its effectiveness has been proven [1]. However, high ratios of symptomatic intracerebral hemorrhages (4–7%) in the rt-PA-injected patients constitute the treatment's most serious adverse effects [1–3]. Reduction of this hemorrhage ratio is strongly desirable. Furthermore, higher therapeutic efficiency resulting in improved prognosis is no less desirable. For these aims of reduction and improvement, one of the most feasible methods is sonothrombolysis in which irradiation with ultrasound enhances the thrombolytic activity of rt-PA specifically at the irradiation site [4–6]. When the enhancement is successfully obtained, a reduction in rt-PA doses is possible, thus helping decrease the hemorrhage ratio.

Sonothrombolysis has been actively studied, and several clinical trials have been conducted. In a CLOTBUST (Combined Lysis of Thrombus in Brain Ischemia Using Transcranial Ultrasound and Systemic t-PA) clinical test [4] with 2 MHz ultrasound, the recanalization rate was improved. In the prognosis after 3 months, however, a statistically significant improvement was not obtained. One of the possible reasons for the 3-month – prognosis result is apparently a problem of low transmittance of 2 MHz ultrasound through the skull. Consequently, a technology to obtain high ultrasound transmittance is favored in sonothrombolysis, not only for 2 MHz but also for other frequencies of ultrasound. A TRUMBI (Transcranial Low-Frequency Ultrasound-Mediated Thrombolysis in Brain Ischemia) trial with 300 kHz ultrasound was stopped prematurely because of an unexpectedly high ratio of cerebral hemorrhages [7]. The reason was not elucidated; however, it was speculated that locally intense spots arose owing to standing waves, which result from the multi-reflection of ultrasound at the inner surface of skulls [7,8].

* Corresponding author.
E-mail address: masajun2093ryo@jikei.ac.jp (M. Yokoyama).

http://dx.doi.org/10.1016/j.ultras.2015.01.017
0041-624X/© 2015 Elsevier B.V. All rights reserved.

To improve the effectiveness and safety [9] of sonothrombolysis, several groups have developed therapeutic devices such as an array transducer composed of both therapeutic and diagnostic ultrasound elements [10], a high-intensity-focused ultrasound probe navigated by MRIs [11–13], and a computer-aided multiple transcranial head frame [14]. For all sonothrombolysis-equipment developments including the above-mentioned examples, estimation of transmittance through human skulls is the most fundamental and important factor for equipment-system designs. For clinical applications, uncertainty of the transmittance is undesirable. If the transmittance is unexpectedly high, the acoustic intensity in the brain will be higher than the anticipated intensity, consequently increasing the risk of cerebral hemorrhages. Likewise, if the transmittance is unexpectedly low, the enhancement effect of thrombolysis will be that much smaller. We believe that the correct estimation of transmittance is one of the most important factors for the effective development of sonothrombolysis therapies. Transmittance varies depending on many factors such as frequency of ultrasound and thickness of bone [15–19]. In particular, White et al. reported interesting frequency-dependent fluctuation behaviors of ultrasound transmittance through the human skull both in calculations and measurements [19]. However, the human skull is not an appropriate measurement sample with which effects of various skull parameters (e.g., thickness, density, sound speed) on ultrasound transmittance are systematically analyzed, because the skull possesses considerably complex structures and various bone thicknesses at different points. In this paper, we use a bone-model plate possessing a representative density of human bone. With this bone plate, we try to systematically analyze transmittance behaviors of ultrasound by varying both the plate parameters and the irradiated ultrasound parameters. In our model, the derivation of which is described later, the transmission of ultrasound fluctuates cyclically according to changes of frequency and plate thickness.

In the past, fluctuations in ultrasound transmittance have not been considered large enough to influence sonothrombolytic therapy's safety or effectiveness. Some previous works reported phase shift of ultrasound with frequency change through a phantom plate [20] or human skull [21] (model calculation). We hypothesize that fluctuations are, in fact, much larger than previously considered, and that the fluctuations significantly affect sonothrombolysis effectiveness and safety. Therefore, we have performed relevant calculations by using a simple model of a bone-phantom plate, and experimentally measured ultrasound transmittance by changing the ultrasound frequency and thickness of the bone-phantom plate.

Many previous studies concerning ultrasound transmission have not investigated the distance between a transducer surface and bone. Clement et al. [22] observed a phase shift of ultrasound through human skull when they moved a transducer. In this case, the authors simultaneously changed both the transducer's location and the distance between the skull surface and the transducer. No published study has conducted a systematic analysis regarding the distance between a transducer surface and bone has not been done. Because water shows similar properties as tissue in terms of density and sound speed, the aforementioned distance can be treated as the thickness of human skull's surrounding skin. Ultrasound reflected at the bone-surface travels back to the transducer and is reflected at the transducer surface, and then, propagates toward the bone again. Owing to interference between the reflected ultrasound and the non-reflected one, transmittance may fluctuate. Therefore, we varied the distance between the transducer surface and the bone-phantom plate in addition to the ultrasound frequency and the plate thickness.

Furthermore, because this undesirable fluctuation results from ultrasound-related reflection and interference, we expect that modulation of ultrasound frequency, which disrupts ultrasound regularity, equalizes the fluctuating transmittance. We have, moreover, experimentally verified this hypothesis. Previously, we used ultrasound modulation [23–25] to reduce standing waves, which constituted a possible cause of cerebral hemorrhages in the TRUMBI trial [22,26,27]. In the current study, we expect that modulation of ultrasound not only can reduce standing waves but also can equalize the fluctuating transmittance of ultrasound through human skulls.

2. Materials and methods

2.1. Experimental setup

We used a transducer (a special-order product; Ueda Japan Radio Corporation, Ueda, Nagano, Japan; Fig. 1A presents a photo of the transducer) possessing a nominal frequency of 500 kHz and a broad bandwidth from 357 kHz to 665 kHz (6-dB down). This transducer was made of 5-mm-thick porous piezoelectric material, and its matching layer was made of SA16 (an epoxy resin). No backing was added. The surface of the transducer formed a flat disk shape whose diameter was 24 mm. A signal from a generator (AFG3102; Tektronix, Beaverton, OR, USA) was amplified with an amplifier (HSA4101; NF Corporation, Yokohama, Kanagawa, Japan) and introduced to the transducer. When we activated the transducer at 500 kHz in water, the wavelength of the ultrasound was approximately 3 mm, and the focused point was 47 mm away from the transducer's surface. (The value of this focused point was calculated according to Eq. (A).)

$$\frac{D^2}{4\lambda}-\frac{\lambda}{4}, \quad (D: \text{transducer diameter}, \lambda: \text{wavelength}), \tag{A}$$

For a model of human temporal skull bone, we used a bone-phantom plate (a special order product; Ueda Japan Radio Corporation, Ueda, Nagano, Japan). The plate size was 50 mm × 70 mm, and the plate thicknesses ranged from 0.6 mm to 4.4 mm at 0.2 mm intervals. Photos of a 2-mm-thick plate are shown in Fig. 1B and C. The plate's surface was placed parallel to the flat disk surface of the transducer. Although thickness of human temporal bone varies from one person to the next, the thicknesses of bone plates lie within a range related to the human temporal bone (3.1 ± 0.9 mm (the average ± S.D.) reported by Wijnhoud et al. [28]. The sound speed of the bone-phantom plates was 2884 m/s (measured according to the ultrasonic pulse method), and its density was 1664 kg/m^3 (measured according to the Archimedes' method). These values are comparable to the human skull bone [16]. The absorption rate of the plate was 0.402 dB/mm/MHz (the average value measured according to the transmission method at 2, 3, 4, and 5 MHz), which was approximately half of a value (0.7 dB/mm/MHz) of human skull bone at 0.56 MHz [29].

A cut piece of human temporal skull bone (3.5 cm × 8.0 cm, Fig. 1D) was purchased through the General Science Corporation Import Company (Tokyo, Japan) from Ets du Docteur Auzoux (Paris, France) on March 2006.

We measured ultrasound intensity passing through the bone-phantom plate with an acoustic intensity measurement system (AIMS) (Onda Corporation, Sunnyvale, CA, USA) equipped with a needle hydrophone having an active tip of 0.4 mm in diameter (HNC-0400; Onda Corporation, Sunnyvale, CA, USA). Special-order calibration was made in a wavelength range from 250 kHz to 1 MHz with 50 kHz intervals in addition to the standard calibration from 1 MHz to 10 MHz. The measurement was conducted with an average acoustic intensity of 200 μsec measurement period. By changing three factors (the frequencies of ultrasound, the thicknesses of the bone-phantom plate, and the distances between the

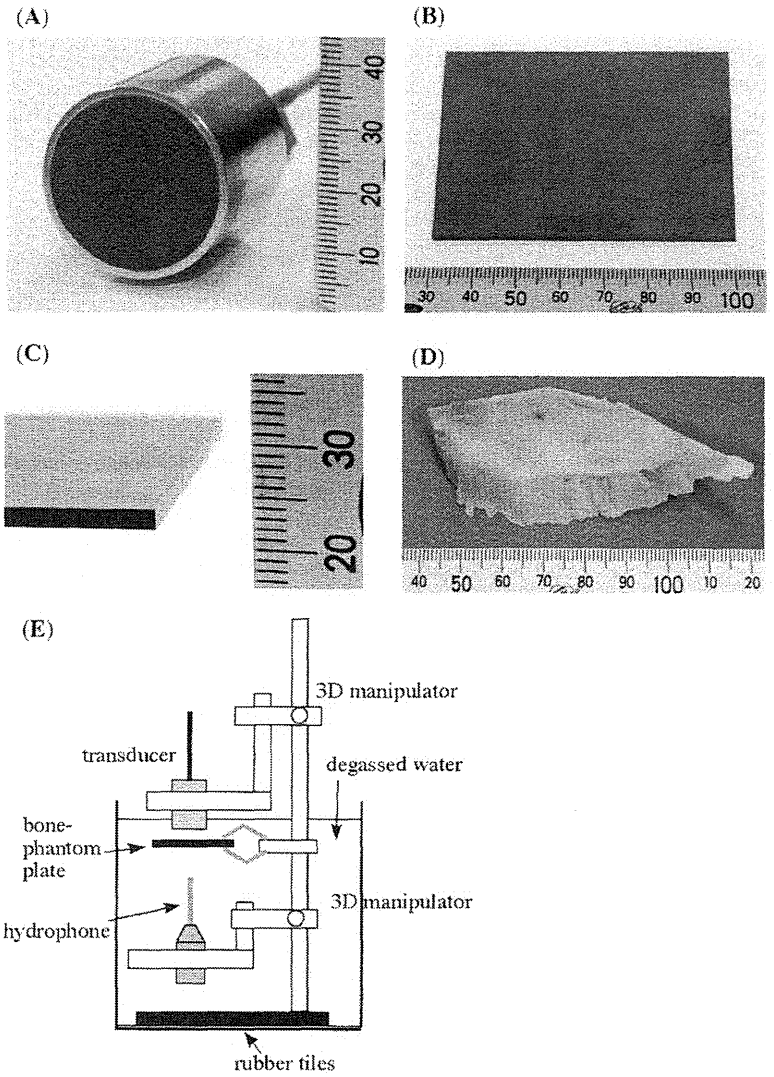

Fig. 1. Experimental samples and device. (A) transducer, (B) surface of a 2-mm-thick bone-phantom plate. (C) close view of the bone-phantom plate for observation of thickness, and (D) cut piece of human temporal skull bone.

transducer surface and the plate), we measured the acoustic intensity of ultrasound passing through the plate.

We used a periodic selection of random frequency (PSRF) method [22] as an ultrasound-modulation method. In this method, various frequencies are chosen randomly, and the selected frequency is irradiated for a certain period T_{PSRF}. The frequency ranged from $(f_0 - D_f)$ to $(f_0 + D_f)$, where f_0 is the carrier frequency and D_f is the frequency deviation (e.g., f_0 = 500 kHz and D_f = 50 kHz). In our experiments, the signal generator read the frequency values from a USB (Universal Serial Bus) drive, in which we stored random value data.

2.2. A calculation based on a multi-layer model

A multi-layer model was used for prediction of the transmittance behaviors [16]. In this model, plane waves are injected into layers, each of which has its own sound speed, density, thickness, and absorption ratio. The waves are reflected or transmitted at each boundary between layers. In this study, we divided the acoustic intensity of the waves passing through all the layers by harnessing the intact waves' acoustic intensity without any plate, and consequently, we obtained a transmittance ratio (τ) in the following formula. Sound speed in water was 1483 m/s, and water density was 998 kg/m^3.

$$\tau = \left[\frac{4Z_wZ_b}{(Z_w+Z_b)^2e^{ik_bd} - (Z_w-Z_b)^2e^{-ik_bd}}\right]^2, \quad (1)$$

(Z_w is acoustic impedance of water, Z_b is acoustic impedance of bone, k_b is wave number in bone, and d is thickness of bone.)

We have taken into account attenuation by complexification of wave numbers, $k \to k - i\alpha$, where α is the attenuation ratio. We used this model to estimate transmission behaviors. In spite of its simplicity (we takes into account neither diffraction nor distribution in the near-field), this model helped clarify basic features of transmission and identify peaks of transmitted intensity. In the model, it can be shown that, in a case of transmission through bone whose absorption is proportional to frequency, the peak frequencies are different for different thicknesses of bone; however, the values of transmittance at peak frequencies are the same for all thicknesses (Fig. 2A).

This formula (1) is derived from ordinal mathematical calculations described below. In this multi-layer model, plane waves

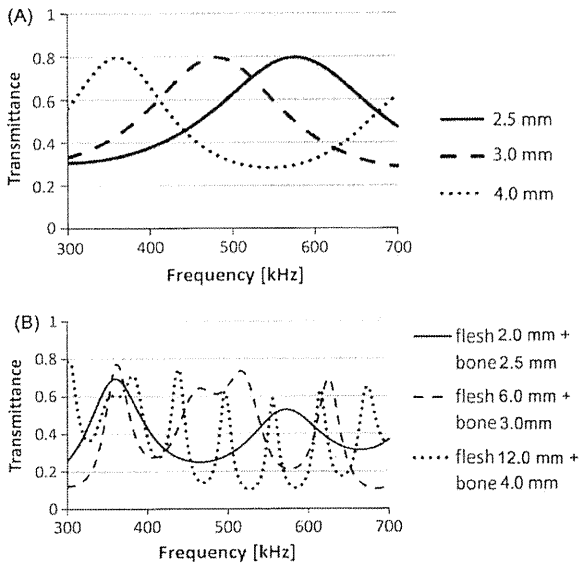

Fig. 2. Calculated transmittance as a function of frequency. (A) The transmittance was calculated with a 3-layer (skin–bone–brain) model. (B) Ultrasound transmittance was calculated with a 4-layer (matching layer–skin–bone–brain) model. The acoustic impedance was 4.8 MRayls. The transmittance is a ratio of the intensity in the brain to the intensity in the matching layer.

propagate in one direction. The pressure of an injected wave can be expressed by $A_0 e^{i(\omega t - k_0 x)}$, where A_0 is pressure amplitude, ω is angular frequency, t is time, k_0 is wave number, and x is a coordinate in the direction of the propagation. Suppose the wave passes through n layers ($n = 1, 2, \ldots$). At boundaries of layers, a part of a wave is reflected, and another part is transmitted. The reflection-to-transmission ratio at the boundary can be determined by the continuity of pressure and particle velocity. In the m-th layer, the wave can be expressed by $A_m e^{i(\omega t - k_m x)} + B_m e^{i(\omega t + k_m x)}$, where k_m is a wave number of the m-th layer. The first term represents a wave propagating in the $+x$ direction while the second term represents a wave propagating in the $-x$ direction. A wave passing through all the layers can be expressed by $A_f e^{i(\omega t - k_f x)}$. We define 2-by-2 matrices $T_{m+1,m}$ and D_m as follows.

$$T_{m+1m} = \begin{pmatrix} \frac{Z_m + Z_{m+1}}{2Z_m} & \frac{Z_m - Z_{m+1}}{2Z_m} \\ \frac{Z_m - Z_{m+1}}{2Z_m} & \frac{Z_m + Z_{m+1}}{2Z_m} \end{pmatrix}, \quad (m = 0, \ldots, n), \tag{2}$$

$$D_m = \begin{pmatrix} e^{-ik_m d_m} & 0 \\ 0 & e^{-ik_m d_m} \end{pmatrix}, \quad (m = 0, \ldots, n), \tag{3}$$

where Z_m is acoustic impedance, and d_m is the thickness of the m-th layer. In the above, $n + 1$ is identified as f. The following formula can be satisfied:

$$\begin{pmatrix} A_f \\ 0 \end{pmatrix} = M \begin{pmatrix} A_0 \\ B_0 \end{pmatrix}, \tag{4}$$

where

$$M = \begin{pmatrix} M_{11} & M_{12} \\ M_{21} & M_{22} \end{pmatrix} \equiv T_{fn} D_n T_{n-1n} D_{n-1} \cdots D_2 T_{21} D_1 T_{10}. \tag{5}$$

Pressure reflection ratio R, pressure transmission ratio T, energy reflection ratio r, and energy transmission ratio τ can be calculated as follows:

$$R \equiv \frac{B_0}{A_0} = -\frac{M_{21}}{M_{22}}, \tag{6}$$

$$T \equiv \frac{A_f}{A_0} = \frac{\det(M)}{M_{22}}, \tag{7}$$

$$r = \left|\frac{M_{21}}{M_{22}}\right|^2, \tag{8}$$

$$\tau = \frac{Z_0}{Z_f}\left|\frac{\det(M)}{M_{22}}\right|^2. \tag{9}$$

In the case of transmission through bone in water, the transmission ratio is expressed in Formula (1).

3. Results

3.1. Fluctuation due to frequency

Fig. 3 shows the frequency dependence of ultrasound transmittance. As shown in Fig. 3A, a 2-mm-thick bone-phantom plate was located at a distance of 1.3 mm from the transducer surface. This 1.3-mm distance is comparable to the thickness of skin on the bone's surface because the acoustic properties of water are almost the same as those of skin. Acoustic intensity was measured at 60 mm from the transducer surface. The transmittance plotted in Fig. 3A is a ratio of the acoustic intensity transmitted through the bone-phantom plate to the acoustic intensity without the bone-phantom plate. A peak was seen near 500 kHz. We predicted the presence of this peak by calculating the multi-layer model for a water layer having a 1.3-mm thickness. The transmittance values near the peak were larger than 1.0. These results indicate that ultrasound intensity rose after transmission through the plate. A possible reason for these larger values is resonance inside the transducer. The reflected wave at the bone-phantom plate entered the transducer, and the oscillation of piezoelectric material was resonantly enhanced. Two additional peaks were present at 340 kHz and 630 kHz. These peaks—corresponding to neither the peaks of the water layer nor the peaks of the bone-phantom plate—seem to have resulted from reflection inside the transducer, which was composed of 5 mm-thick piezoelectric material. Fig. 3B

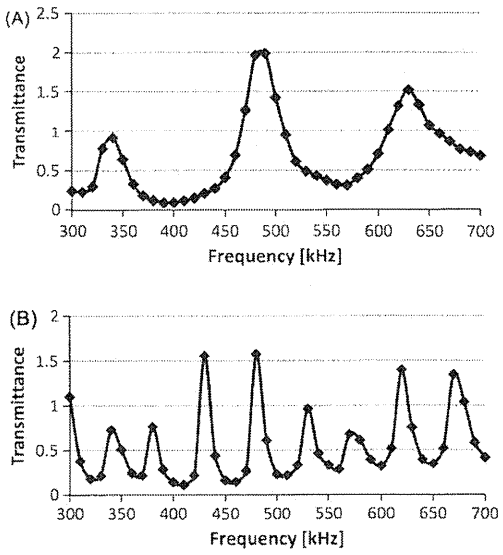

Fig. 3. Measured frequency dependence of ultrasound transmittance. Transmittance is a ratio of acoustic intensity through the bone-phantom to intensity without the bone-phantom. Bone-phantom thickness was 2 mm, and distance between the transducer surface and the bone-phantom was 1.3 mm for (A) and 12 mm for (B). A hydrophone was located 60 mm from the transducer surface.

presents plots that we obtained involving a water-layer thickness of 12 mm, which is close to the average skin-thickness of older Japanese at the temporal region recently measured on MRI images (data not shown. A reference [30] reported 9.5 ± 2.6 mm as the average value for 5 young healthy volunteers of 29–36 years old.) Again, the transmittance significantly fluctuated depending on frequency, and the transmittance value exceeded 1.0 at several peaks. In this case, the interval between peaks was approximately 50 kHz, which was shorter than Fig. 3A's 2-mm-thick case. This finding is consistent with our calculation that the interval is inversely proportional to the water-layer thickness. Differences between the local maximums and the local minimums were significantly large, and the ratio between the maximum and the minimum was 14 (maximum: 1.57 at 480 kHz, minimum: 0.113 at 410 kHz).

3.2. Fluctuation due to skin-thickness

By changing water-layer thickness, which corresponds to skin thickness, we measured transmittance. First, we calculated transmittance using a multi-layer model, and the results are shown in Fig. 4. The model consisted of a transducer's matching layer (infinite medium model of 4.8 MRayls acoustic impedance), a water layer, a bone layer, and another water layer. In the boundary condition, we assume continuous pressure and particle velocity at the boundaries between two layers. Transmittance increment and decrement were repeated with a cycle of 1.5 mm. This cyclic behavior results from reflection at the transducer surface.

Then, we measured transmittance by changing the distance between the transducer surface and the bone-phantom plate. Results are shown in Fig. 5A and B. The distance ranges from 0 to 4.0 mm in Fig. 5A, while it ranges from 11.0 mm to 12.8 mm in Fig. 5B. As the distance increased, the transmittance underwent a cyclic change. For these figures, we conducted measurements at 60 mm from the bone-phantom plate. We found that these results agreed well with the calculated results shown in Fig. 4. The cycle was approximately 1.5 mm in the two cases. The ratio of the local maximum to the local minimum in the region within a 4-mm distance differed from the ratio in the region whose distance was greater than 11 mm. The possible reason for this difference is that plane-wave approximation is not valid when distances are large.

The above-described results (Figs. 3A and B, and 5A and B) were obtained in measurements with a hydrophone placed at a distance of 60 mm from the transducer surface. Fig. 5C represents the transmittance measured at various hydrophone distances in cases where water-layer thickness was 0.64 mm, 1.3 mm, and 1.6 mm. For all the cases, the intensity change was very small (about 60 mm). This finding is inconsistent with the assertion that the cyclic behaviors described in Fig. 5A and B come from significant distance-dependent fluctuations in ultrasound intensity.

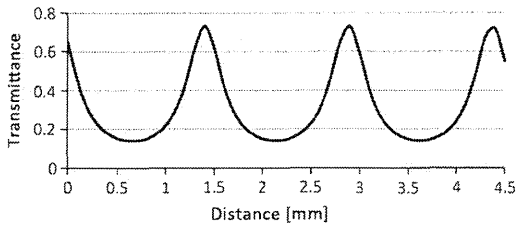

Fig. 4. Calculated ultrasound transmittance as a function of distance between the transducer and the bone-phantom plate. Acoustic impedance is normalized in the matching layer. Ultrasound frequency was 500 kHz. Acoustic impedance of the matching layer was 4.8×10^6 Rayls.

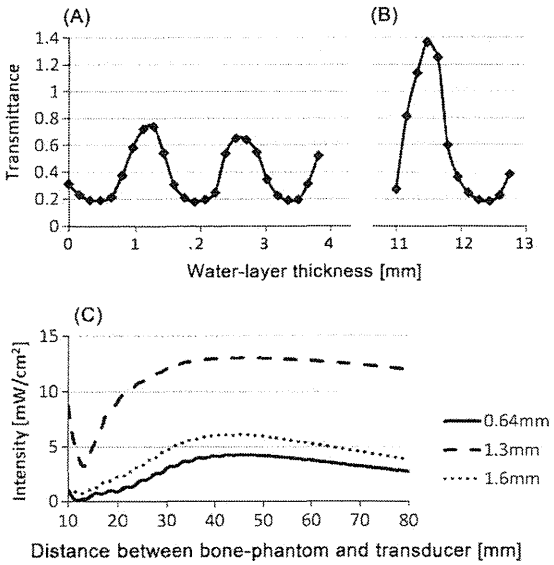

Fig. 5. Measured change of ultrasound transmittance as a function of distance between transducer and bone-phantom plate. Frequency was 500 kHz. Bone-phantom thickness was 2 mm for (A) and (B). In (A) and (B), a hydrophone was located 60 mm from the bone-phantom plate. In (C), intensity distribution is shown at various hydrophone distances from the transducer. Voltage was 13.3 Vpp.

3.3. Fluctuation due to bone-thickness

Next, we examined the dependence of ultrasound transmittance on bone-phantom plate thickness. Results are shown in Fig. 6. The calculations in our multi-layer model predicted a local maximum intensity at around 3 mm and an approximately 3-mm cycle. In Fig. 6, a maximum peak at 2.8 mm and an approximate 3-mm periodical cycle were observed. These facts indicate good consistency between the calculations and the measurements. On the other hand, this finding is inconsistent with the assertion that ultrasound transmittance is higher for thinner bones. Many researchers and clinicians seem to believe that this assertion is true in all clinical practices of sonothrombolysis, ultrasound diagnosis, and other ultrasound-utilized therapies. We also observed small shoulders at 1.6 mm and 3.2 mm, indicating 1.6-mm-cyclic behavior. These shoulders are not predicted in the model calculation. We repeated measurements several times and found that the dip was reproducible. The reason for these shoulders' appearance is unknown. We considered several possibilities: material differences, generation of such high-frequencies as 1 MHz (double the frequency of 500 kHz), and non-linear absorption; however, we experimentally disproved these possibilities. A change in hydrophone-position did not eliminate the dip. We used 650-kHz sinusoidal waves and observed a smooth transition of transmittance at a thickness of about 3.2-mm (data not shown). We also disproved the possibility that ultrasounds at such high frequencies as 1 MHz arising from

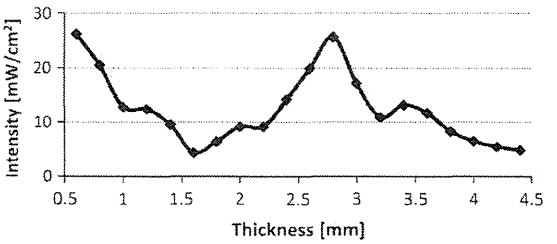

Fig. 6. Measured dependence of ultrasound transmittance on bone-phantom thickness. Frequency: 500 kHz; voltage: 20 Vpp; distance between transducer and surface: 12 mm. A hydrophone was placed 60 mm from the transducer.

waveform distortion contributed to the dip at 3.2 mm. We observed the Fourier component of transmitted waves by oscilloscope (TDS3012; Tektronix, OR, USA) and found that the 1-MHz component was 37 dB smaller than the 500-kHz component. Such a small 1-MHz component is negligible for consideration of the prominent dip at 3.2 mm. We further disproved the non-linear effect: When we activated the transducer using different voltages (Fig. 7A), the acoustic intensity of ultrasound passing through the bone-phantom plate (normalized by the acoustic intensity of freely propagating waves) was the same in spite of different voltages (Fig. 7B). We cannot clarify the reason for the dip. However, we can infer that the dip position is relevant to ultrasound wavelength because the dip was produced at a 4.0-mm thickness when we used 400 kHz ultrasound (Fig. 8). Unknown phenomena seemed to occur in the bone-phantom plate for certain wavelengths and for certain bone-phantom plate thicknesses. Although the reason for the appearance of the shoulders is presently unclear, they did not influence our finding that intensity fluctuated up to a 3-mm maximum range and in a 3-mm cycle, as the calculation predicted. The ratio of the highest transmittance to the lowest was 6.0. This ratio is considered unfavorably large for clinical applications, since acoustic intensity in the brain fluctuates significantly.

3.4. Fluctuation due to multiple factors

Fig. 2 shows our calculation of ultrasound transmittance as a function of frequency. And as shown in Fig. 2A, we evaluated the transmittance by using a 3-layer model composed of water (skin), bone, and water (brain) layers. In this 3-layer model, the incident ultrasound wave propagates through skin of infinite thickness. We focus on the effect of bone-thickness. Peak frequency was observed to fluctuate with bone thickness. When we used a 500-kHz sinusoidal wave, ultrasound easily passed through a 3.0-mm-thick bone plate because this thickness (3.0 mm) was approximately half the wavelength (6 mm) of the 500 kHz sinusoidal wave (on the assumption of a sound speed at 3000 m/s in the bone-phantom plate). By contrast, when the bone thickness was slightly changed to 2.5 mm or 4 mm, the peak position changed. As shown in Fig. 2B, we took into account both bone thickness and skin thickness. The transmittance was calculated in a 4-layer model (matching layer–skin–bone–brain). We observed that transmittance fluctuated depending on skin thickness and bone thickness. Consequently, suitable frequency differs individually, and it is impossible to choose one frequency suited for every individual. Additionally, when ultrasound is used at one frequency in clinical practices, slight differences in skin- and bone-thickness will result in big differences in transmittance. Too strong an ultrasound intensity in the brain can cause adverse effects such as hemorrhages, while thrombolytic efficacy is not obtained in too weak a transmitted ultrasound intensity.

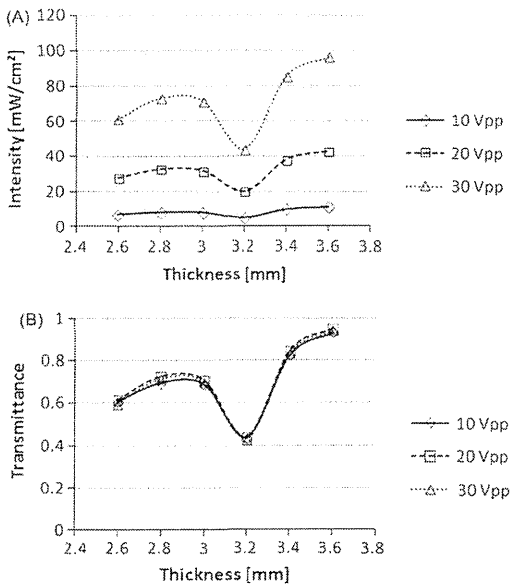

Fig. 7. Influence of activating voltage change. The frequency was 500 kHz. The distance between a transducer surface and a bone-phantom plate was 6 mm. A hydrophone was located 60 mm from the transducer surface. In (A), acoustic intensity is plotted. In (B), transmittance is plotted. The transmittance is a transmitted intensity value divided by intensity without a plate. The values without a plate were 11.6 mW/cm^2 for 10 Vpp, 44.9 mW/cm^2 for 20 Vpp, and 102.1 mW/cm^2 for 30 Vpp.

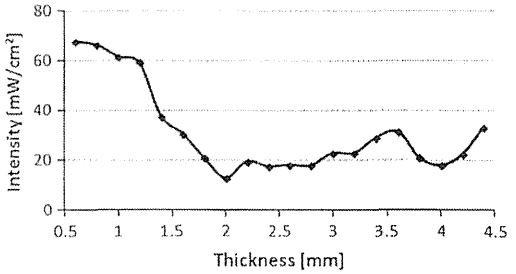

Fig. 8. Acoustic intensity in the 400-kHz case. The voltage was 20 Vpp. Distance between a transducer and a bone-phantom plate was 6 mm. A hydrophone was placed at 60 mm from the transducer surface.

3.5. Equalization by modulation of ultrasound frequency

As shown in Fig. 9, we experimentally compared the transmittance of a sinusoidal wave with that of a wave modulated by the PSRF method, which changes frequency randomly at certain time intervals. We changed the distance between the transducer and the 2-mm-thick bone-phantom plate (see Fig. 9A). We set

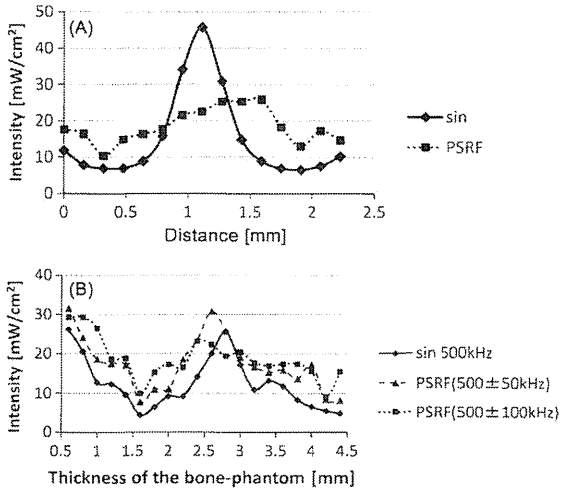

Fig. 9. Equalization (measured) of ultrasound transmittance by means of PSRF. (A) We changed the distance between the transducer surface and the bone-phantom plate. Thickness of bone-phantom: 2 mm; voltage: 20 Vpp; frequency: 500 kHz (sinusoidal wave) and 500 ± 100 kHz (PSRF). We changed the PSRF frequency every 1 μs. A hydrophone was placed 60 mm from the bone-phantom plate. (B) We changed the thickness of the bone-phantom plate. The distance between the transducer surface and the bone-phantom plate was 12 mm. A hydrophone was located 60 mm from the transducer. Applied voltage was 20 Vpp.

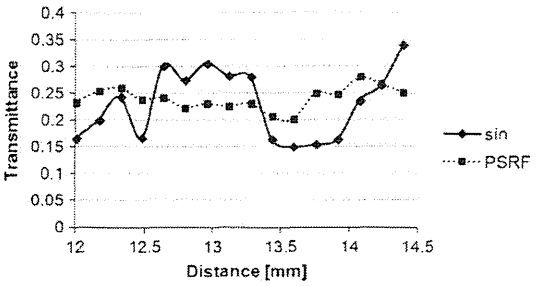

Fig. 10. Equalization (measured) of ultrasound transmittance by means of PSRF for a cut piece of human temporal skull bone. We changed the distance between the transducer surface and the surface of the bone piece. Voltage: 20 Vpp; frequency: 500 kHz (sinusoidal wave) and 500 ± 100 kHz (PSRF). We changed the PSRF frequency every 1 μs. A hydrophone was placed 60 mm from the piece bone.

T_{PSRF} = 1 μs and D_f = 100 kHz for the PSRF method. The distance-related transmittance fluctuation was smaller in the PSRF case than in the sinusoidal-wave case. The ratio of the highest transmittance to the lowest one was 7.0 in the sinusoidal case and 2.5 in the PSRF case. The transmittance was substantially equalized in the PSRF case. By changing plate thickness, we compared transmittance (see Fig. 9B). We observed that the thickness-related transmittance fluctuation was smaller for the modulated waves than for the sinusoidal waves, and was smallest for the modulated waves possessing a broad frequency bandwidth. The ratio of maximum to minimum transmittance was 6.0 for sinusoidal waves (500 kHz), 4.1 for a PSRF scenario (500 ± 50 kHz), and 3.3 for another PSRF scenario (500 ± 100 kHz).

In the next step, we measured ultrasound transmittance through a cut piece of human temporal skull bone by changing the distance between the transducer and the surface of the bone piece. Fig. 10 plots the transmittance values of the 500 kHz sinusoidal wave (sin) and the PSRF modulated wave (PSRF, 500 ± 100 kHz) are plotted. Although changes to the transmittance values were more complex than the changes in the phantom-plate case (Fig. 4A and B), we observed a considerably large fluctuation with the sinusoidal wave for this bone piece. In this measured distance range, the ratio of the highest transmittance to the lowest one was 2.3. This ratio was significantly reduced to 1.4 when the modulated wave was irradiated. These results indicate that considerably large fluctuations in ultrasound transmittance can happen in the human skull. In future research, we would like to perform detailed measurements of the human skull's fluctuation behaviors to identify, with exactitude, two important factors: first, the fluctuation's significance for sonothrombolysis, and second, whether the modulation technique is effective in reducing the fluctuation in clinical applications.

4. Discussion

We found that ultrasound transmittance through a bone-phantom plate significantly fluctuated with changes in ultrasound frequency, bone-thickness, and skin-thickness. Additionally, we clarified that skin-thickness played an important role in transmittance. Previous research did not address skin-thickness effects on ultrasound therapies. By comparing Fig. 1A and B, we can observe the effects of skin-thickness. The significant fluctuations in transmittance may impede the development of safe and effective transcranial therapeutic devices.

Fry et al. reported [16] that reflections of ultrasound through the human skull fluctuated but that transmitted ultrasound intensity did not fluctuate. In the field of sonothrombolysis, a general assumption has been that transmittance through the human skull is lower both for thicker skull bone and at higher ultrasound frequencies. White et al. [18] reported transmission behaviors through a human skull on the basis of ultrasound-frequency changes. They calculated and measured the transmittance at 17 points along a human skull in a frequency range extending from 600 kHz to 1.4 MHz. The average bone thickness was 6.1 mm. Their calculated result for the average 6.1-mm thickness is shown as a dotted line in Fig. 11A. They observed cyclic fluctuation behavior. However, this cyclic fluctuation was buried in the more dominant trend of decreases in frequency-related transmittance. Our calculated results are plotted as a solid line in this figure. The solid line exhibits only the cyclic fluctuation without the decreasing frequency-related trend. Differences between the two plots result from two factors: one is a difference in the absorption rate of bone, as our calculation involves 0.402 dB/mm/MHz, whereas $-123 + 3.559 \times 10^{-4}$ f Np/m is involved in reference [18]; the second difference concerns thickness, as our calculation involves 2.0 mm, whereas 6.1 mm is involved in reference [18]. Our calculation using a thinner bone model is suitable for sonothrombolysis through a temporal window, while White's reference involved transcranial ultrasound therapy through all the surface points on the skull. Fig. 11B compares measured transmittance plots. Our results (solid line) reveal only cyclic fluctuation, while White's

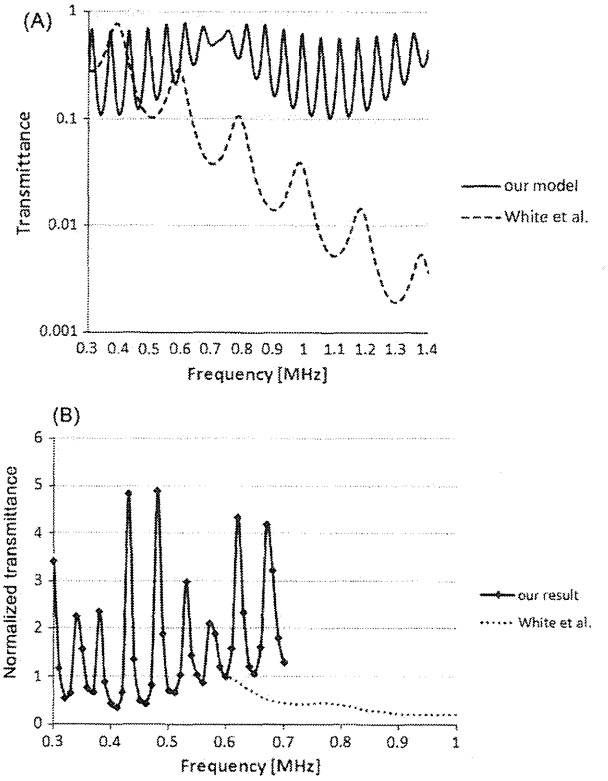

Fig. 11. Comparisons between our results and reference [19] in calculations (A) and in measurements (B). (A) Frequency dependence of transmittance (model calculation). The solid line derives from our 4-layer model consisting of a matching layer (4.8 MRayls), a water layer (998 kg/m^3, 1483 m/s), a bone-phantom plate (1664 kg/m^3, 2884 m/s, 0.402 dB/mm/MHz), and a water layer. The thickness of the bone-phantom plate was 2 mm, and the distance between the transducer surface and the bone-phantom plate was 1.3 mm. The broken line derives from a result in the propagation model used in reference 13. The model ultrasound transmitted through a 7.1-mm homogeneous layer (2132 kg/m^3, 2800 m/s, $\alpha = -123 + 3.559 \times 10^{-4}$ f) in water (1000 kg/m^3, 1500 m/s). (B) Measurements of ultrasound transmittance behaviors. The solid line represents our results shown in Fig. 3(B), while the dotted line represents results from reference [19]. In this figure, the transmittance is normalized by a value of 0.6 MHz.

results (dotted line) exhibit the trend of frequency-related decreases. The cyclic fluctuation is scarcely observed on the dotted line. The significant differences in Fig. 10A and B indicate the importance of the substantial cyclic fluctuation of ultrasound transmittance at least for sonothrombolytic therapy through the temporal window.

We obtained our results in experiments using a bone-phantom plate and model calculations based on multi-layers. Since human skull bone has a complex geometrical structure with inhomogeneous density degrees, fluctuations may be less than those obtained in this work. Evaluation of fluctuations with human skulls and temporal bone merits further attention, and both this type of evaluation and fluctuation-reduction technologies are very important for clinical designs of safe and effective sonothrombolytic therapies.

In this paper, we showed that modulation of ultrasound frequency reduced fluctuations. Because transmittance significantly fluctuated with frequency (Fig. 2), we tried (successfully) to equalize the transmittance fluctuations by using the PSRF method of frequency modulation. As shown in Fig. 9, the broader a frequency deviation, the greater the equalization effect. If the medical community were to further broaden frequency deviation even more so, the equalization of transmittance might improve. However, broader frequency deviation is not always preferred. A frequency far from the center frequency of a transducer will not effectively convert into ultrasound, and this outcome can generate heat harmful to living bodies will be generated. Taking into account the above-mentioned facts, we should identify an optimal balance between equalization and transducer design.

We experimentally verified that ultrasound transmittance changed according to skin-thickness, frequency, and bone-thickness. Since frequency dependence is different from individual to individual, we cannot choose a single frequency suitable for every individual. In the absence of a single optimal frequency, the equalization of the transmittance through ultrasound modulation is a highly effective and important methodology for sonothrombolytic therapy.

Acknowledgements

The authors would like to acknowledge a Grant for Research on Advanced Technology (H21-008) and a Health Labor Sciences Research Grant (H24-006) from the Ministry of Health, Labor, and Welfare of Japan.

References

[1] The National Institute of Neurological Disorders and Stroke rt-PA Stroke Study Group, Tissue plasminogen activator for acute ischemic stroke, N. Engl. J. Med. 333 (1995) 1581–1587.
[2] T. Yamaguchi, E. Mori, K. Minematsu, J. Nakagawara, K. Hashi, I. Saito, Y. Shinohara, Japan Alteplase Clinical Trial (J-ACT) Group, Alteplase at 0.6 mg/kg for acute ischemic stroke within 3 hours of onset: Japan Alteplase Clinical Trial (J-ACT), Stroke 37 (2006) 1810–1815.
[3] W. Hacke, M. Kaste, E. Bluhmki, M. Brozman, A. Dávalos, D. Guidetti, V. Larrue, K.R. Lees, Z. Medeghri, T. Machnig, D. Schneider, R. von Kummer, N. Wahlgren, D. Toni, ECASS investigators, thrombolysis with alteplase 3 to 4.5 hours after acute ischemic stroke, N. Engl. J. Med. 359 (2008) 1317–1329.
[4] A.V. Alexandrov, C.A. Molina, J.C. Grotta, Z. Garami, S.R. Ford, J. Alvarez-Sabin, J. Montaner, M. Saqqur, A.M. Demchuk, L.A. Moyé, M.D. Hill, A.W. Wojner, CLOTBUST investigators, ultrasound-enhanced systemic thrombolysis for acute ischemic stroke, N. Engl. J. Med. 351 (2004) 2170–2178.
[5] K. Barlinn, G. Tsivgoulis, C.A. Molina, D.A. Alexandrov, M.E. Schafer, J. Alleman, A.V. Alexandrov, TUCSON investigators, exploratory analysis of estimated acoustic peak rarefaction pressure, recanalization, and outcome in the transcranial ultrasound in clinical sonothrombolysis trial, J. Clin. Ultrasound 41 (2013) 354–360.
[6] J. Eggers, I.R. König, B. Koch, G. Händler, G. Siedel, Sonothrombolysis with transcranial color-coded sonography and recombinant tissue-type plasminogen activator in acute middle cerebral artery main stem occlusion. Results from a randomized study, Stroke 39 (2008) 1470–1475.
[7] M. Daffertshofer, A. Gass, P. Ringleb, M. Sitzer, U. Sliwka, T. Els, O. Sedlaczek, W.J. Koroshetz, M.G. Hennerici, Transcranial low-frequency ultrasound-mediated thrombolysis in brain ischemia: Increased risk of hemorrhage with combined ultrasound and tissue plasminogen activator – results of a phase II clinical trial, Stroke 36 (2005) 1441–1446.
[8] Z. Wang, M.A. Moehring, A.H. Voie, H. Furuhata, In vitro evaluation of dual mode ultrasonic thrombolysis method for transcranial application with an occlusive thrombosis model, Ultrasound Med. Biol. 34 (2008) 96–102.
[9] J. Shimizu, T. Fukuda, T. Abe, M. Ogihara, J. Kubota, A. Sasaki, T. Azuma, K. Sasaki, K. Shimizu, T. Oishi, S. Umemura, H. Furuhata, Ultrasound safety with midfrequency transcranial sonothrombolysis: preliminary study on normal Macaca monkey brain, Ultrasound Med. Biol. 38 (2012) 1040–1050.
[10] T. Azuma, M. Ogihara, J. Kubota, A. Sasaki, S. Umemura, H. Furuhata, Dual-frequency ultrasound imaging and therapeutic bilaminar array using frequency selective isolation layer, IEEE Trans. Ultrason. Ferroelectr. Freq. Control 57 (2010) 1211–1224.
[11] K. Hynynen, N. McDannold, G. Clement, F.A. Jolesz, E. Zadicario, R. Killiany, T. Moore, D. Rosen, Preclinical testing of a phased array ultrasound system for MRI-guided noninvasive surgery of the brain – a primate study, Eur. J. Radiol. 59 (2006) 149–156.
[12] K. Hynynen, G. Clement, Clinical applications of focused ultrasound – the brain, Int. J. Hyperther. 23 (2007) 193–202.
[13] C. Yiallouras, C. Damianou, Review of MRI positioning devices for guiding focused ultrasound systems, Int. J. Med. Robot (in press), http://dx.doi.org/10.1002/rcs.1601.
[14] M.E. Shafer, J. Alleman, A. Alexandrov, K. Barlinn, Development of an operator independent ultrasound therapeutic device for stroke treatment, in: 2012 IEEE International Ultrason, Symposium Proceedings, 2012, pp. 1948–1951.
[15] A.Y. Amm, T.D. Mast, I.H. Huang, T.A. Abruzz, C.C. Coussios, G.J. Shaw, C.K. Holland, Characterization of ultrasound propagation through ex-vivo human temporal bone, Ultrasound Med. Biol. 34 (2008) 1578–1589.
[16] G. Bouchoux, R. Shivashankar, T.A. Abruzzo, C.K. Holland, In silico study of low-frequency transcranial ultrasound fields in acute ischemic stroke patients, Ultrasound Med. Biol. 40 (2014) 1154–1166.
[17] F.J. Fry, J.E. Barger, Acoustical properties of the human skull, J. Acoust. Soc. Am. 64 (1978) 423–457.
[18] S. Pichardo, V.W. Sin, K. Hynynen, Multi-frequency characterization of the speed of sound and attenuation coefficient for longitudinal transmission of freshly excised human skulls, Phys. Med. Biol. 56 (2011) 219–250.
[19] P.J. White, G.T. Clement, K. Hynynen, Local frequency dependence in transcranial ultrasound transmission, Phys. Med. Biol. 51 (2006) 2293–2305.
[20] J. Aarnio, G.T. Clement, K. Hynynen, A new ultrasound method for determining the acoustic phase shifts caused by the skull bone, Ultrasound Med. Biol. 31 (2005) 771–780.
[21] M. Hayner, K.J. Hynynen, Numerical analysis of ultrasonic transmission and absorption of oblique plane waves through the human skull, J. Acoust. Soc. Am. 110 (2001) 3319–3330.
[22] G.T. Clement, J. Sun, K. Hynynen, The role of internal reflection in transskull phase distortion, Ultrasonics 39 (2001) 109–113.
[23] H. Furuhata, O. Saito, Comparative study of standing wave reduction methods using random modulation for transcranial ultrasonication, Ultrasound Med. Biol. 39 (2013) 1440–1450.
[24] S.C. Tang, G.T. Clement, Acoustic standing wave suppression using randomized phase-shift-keying excitations, J. Acoust. Soc. Am. 126 (2009) 1667–1670.
[25] S.C. Tang, G.T. Clement, Standing wave suppression for transcranial ultrasound by random-modulation, IEEE Trans. Biomed. Eng. 57 (2010) 203–205.
[26] C. Baron, J.F. Aubry, M. Tanter, S. Meairs, M. Fink, Simulation of intracranial acoustic fields in clinical trials of sonothrombolysis, Ultrasound Med. Biol. 35 (2009) 1148–1158.
[27] J. Song, A. Pulkkinen, Y. Huang, K. Hynynen, Investigation of standing wave formation in a human skull for a clinical prototype of a large-aperture, transcranial MR-guided focused ultrasound (MRgFUS) phased array: an experimental and simulation study, IEEE Trans. Biomed. Eng. 59 (2012) 435–444.
[28] A.D. Wijnhoud, M. Franckena, A. van der Lugt, P.J. Koudstaal, E.D. Dippel, Inadequate acoustical temporal bone window in patients with a transient ischemic attack or minor stroke: role of skull thickness and bone density, Ultrasound Med. Biol. 34 (2008) 923–929.
[29] T.F. Hueter, Ultrasonic absorption measurements in human skull bone and their dependence upon frequency, Naturwiss 39 (1952) 21–22.
[30] F. Babiloni, C. Babiloni, F. Carducci, M. Del Gaudio, P. Onorati, A. Urbano, A high resolution EEG method based on the correction of the surface Laplacian estimate for the subject's variable scalp thickness, Electroencephalogr. Clin. Neurophysiol. 103 (1997) 486–492.

R002879364995